Computational Geometry in Medical Applications

Camilo Andrés Cortés Acosta

Computational Geometry in Medical Applications

Student: Camilo Andrés Cortés Acosta
Supervisor: Prof. Dr. Ing. Oscar Ruiz

SCHOOL OF ENGINEERING
UNIVERSIDAD EAFIT
MEDELLÍN, COLOMBIA

SUBMITTED IN PARTIAL FULFILLMENT OF THE REQUIREMENTS FOR A MASTERS OF SCIENCE DEGREE IN ENGINEERING FROM THE SCHOOL OF ENGINEERING, UNIVERSIDAD EAFIT.

September 2012

Acknowledgements

I want to thank my family for their constant support, efforts, encouragement and love. I thank my advisor, Prof. Oscar Ruiz, for his trust, support, guidance, and for giving me the opportunity to get involved with CAD CAM CAE Laboratory and perform the M.Sc Programme of Engineering at Univerdad EAFIT. Also, I want to thank Prof. Diego Acosta for his accompaniment and efforts. I want to express my gratitude to my friends and colleagues at the CAD CAM CAE Laboratory, specially to Mauricio Aristizábal, Jorge Correa, Maria Camila Osorno and Manuel Espinosa, who contributed to my master studies and thesis. My grateful acknowledgements to EAFIT University for their financial support for my master studies and the research projects in which I have participated.

Special thanks to Dr. Jorge Posada, Dr. Shabs Rajasekharan and Dr. Alessandro de Mauro for giving me the opportunity to perform my master's graduation project at Vicomtech, also, for their support and guidance. Many thanks to my friends and colleagues at Vicomtech, specially to John Congote, Carlos Toro, Luis Kabongo and Iñigo Barandiaran, Digna Gonzalez and Tassilo Glander for their accompaniment and advice.

This work has been partially supported by the Colombian Council for Science and Technology -Colciencias-. VICOMTech Institute and CAD/CAM/CAE Laboratory - Universidad EAFIT.

Contents

List of Figures

Introduction

The integration of computer based tools and systems to the workflow of several medical procedures has allowed the doctors to obtain valuable information for the diagnosis stage and to enhance their capabilities during the interventional procedures. These new solutions based on geometric modeling, computer vision and robotics, among others, ease the identification and extraction of information of the anatomical structures of interest and help the doctors to perform safer interventions, improving the outcomes of the different treatments.

Image guided surgery constitutes one of the fields where all of the mentioned technologies can be merged. After the medical imaging stage (e.g. ultrasound, CT, MRI), the organs and other anatomical structures can be reconstructed, providing a 3D model of the patient, which is used to identify the regions of interest and to plan the surgery. During the intervention, these preoperative models can be merged with real images of the patient, obtained for example by endoscopic video or ultrasound, using augmented reality techniques, helping the surgeon to locate the targets of the surgery. Depending on the surgical procedure, robotic systems can perform a series of autonomous tasks based on the preoperative plan. In other cases, the surgeon performs the intervention using a telerobotic platform that directly handles the surgical instruments and receives the movement commands from the surgeon through haptic devices. Additional force signals can be provided to the surgeon through the haptic device during the robotic surgery, in order to help him following a defined trajectory or to avoid undesired contacts with critical structures.

Several concepts and methods that help to solve the challenges involved in the different stages of image guided surgery are based on the field of computational geometry. Computational geometry is the study of algorithms and data structures for the solution of problems that can be stated in terms of geometry. The devised solutions presented in this work involve several elements of combinational, numerical and stochastic computational geometry.

The structure of this work consists on a compilation of developments performed at the CAD CAM CAE Laboratory of Universidad EAFIT (Medellin, Colombia) and VICOMTech research center (Donostia - San Sebastian, Spain). In this way, each one of the mentioned applications constitutes a chapter of this document. Each development contributes to some of the methods and algorithms that are implemented to undertake the medical tasks described previously.

Chapter 1 is a literature review of the state of the art of medical interventional telerobotic platforms with force feedback. This was motivated by the development of a telerobotic system, with force feedback capability at VICOMTech institute, given that there

are not commercial telesurgical systems that implement this feature. The results of this research have been used as guidelines for the architecture, control and implementation of such telerobotic platform. This article gives an overview of the main challenges involved in the areas of force measurement and estimation, master and slave robot desing, haptic rendering and bilateral control. Also, a taxonomy of the recent developed telerobotic platforms is presented. Although the computational geometry concepts involved in implementing such platforms are not discussed in this review, several of them are closely related and are neccesary to understand how these systems work. In robotics, the forward and inverse kinematics are solved using geometric relationships, modelling the robot's links as rigid bodies subjected to geometric constrains. For the motion planning problem, splines are widely used to model the motion in joint-space and task-space, pursuing the velocity and acceleration continuity during the motion. In master-slave systems, geometric transformations are used to stablish the desired position and orientation of the slave robot, as well as for the implementation of motion scaling. When the master console is able to provide haptic feedback, virtual forces can be generated in order to improve the system performance. To generate these virtual forces collision detection and force response algorithms are used. These algorithms are based on the geometric properties of the collided objects. In this way, numeric as well as combinational computational geometric concepts are present here.

Chapter 2 describes an image dataset and evaluation framework to assess the performance of keypoint extraction and feature descriptor matching algorithms. The need for normalized data and protocols to perform such evaluations motivated this development at VICOMTech institute. The mentioned algorithms play a key role in several domains, such as 3D reconstruction, object recognition, camera tracking and augmented reality. This techniques are mainly implemented during surgery for processes such as patient registration, endoscope automatic positioning and visual servoing, among others. Central to the process of generating an image dataset for the assesment of keypoint extractors mechanisims is the concept of geometric transformations. In this case, the generated images are related by an homography, which constitutes the groud-truth data to permorm the evaluations of the different algorithms. For this application, the positioning of the camera was performed using a robotic arm, which also involves the use of geometric transformations to define the camera trajectory in task-space. The geometric transformations field is part of the combinational computational geometry area.

Chapter 3 shows an application that deals with the problem of curve reconstruction from noisy point samples using parametric curves. The lack of a formal characterization and a sensitivity analysis of this problem from the mathematical optimization perspective motivated this work at CAD CAM CAE Laboratory of the Universidad EAFIT. The mentioned application is needed for surface reconstruction in many fields, including the processing of medical images, which is of prime importance for the surgery planning stage. As part of the results of this research, an optimized curve fitting method is provided. The outcomes of the sensitivity analysis allowed determining how the parameters involved in the optimization problem affect the results. Since the curves are reconstructed using B-splines, this geometric modeling application, involves the numeric computational geometry subfield. Also, this problem requires the application of combinatorial geometry, for example, to solve the problem of finding the minimum distance between the curve and cloud points.

CHAPTER 1

State-of-the-Art in medical interventional teleoperated robotic systems with force feedback

CONTEXT: A project to develop a telerobotic system, with force feedback capability, which is to be used in several medical applications is being developed at VICOMTech institute. As an initial stage of these development, a deep literature review of the state of the art of medical telerobotic platforms was conducted. These survey was focused on interventional systems with force feedaback, which offer several benefits over platforms that only provide visual cues. The results of this research have been used as guidelines for the architecture, control and implementation of the telerobotic platform. This paper includes material obtained by the technical advances in the mentioned project to explain some of the concepts presented in the survey.

This work has been founded by Universidad EAFIT, the Colombian Council of Research and Technology (COLCIENCIAS) and VICOMTech Institute. Camilo Cortes, research assistant under my direction in the CAD CAM CAE Laboratory, conducted this research and programmed the required algorithms for the project. The contributions of this work have been submmited to The International Journal of Medical Robotics and Computer Assisted Surgery and are pending for publication.

- Camilo Cortés[1,2]
- Alessandro de Mauro[2]
- Oscar E. Ruiz[1]

[1] CAD CAM CAE laboratory, Universidad EAFIT
Carrera 49 No 7 Sur - 50, Medellín, Colombia
[2] eHealth and Biomedical Applications, VICOMTech-IK4
Mikeletegi Pasealekua 57, San Sebastián, Spain

As co-authors of such publication, we give our permission for this material to appear in this document. We are ready to provide any additional information on the subject, as needed.

Prof. Dr. Eng. Oscar E. Ruiz
oruiz@eafit.edu.co
Coordinator CAD CAM CAE Laboratory
EAFIT University, Medellin, COLOMBIA

ABSTRACT. **Background** Telesurgical systems enhance surgeon's capabilities, providing high positioning accuracy and dexterity. The integration of haptic feedback into these systems increases the procedure's safety, helping to prevent errors. However, there are currently no commercial systems that implement this feature.

Methods Recent advances in the implementation of force feedback in teleoperated systems for several interventional medical procedures are presented. Additionally, the fields of contact force measurement and estimation, bilateral control, and master and slave devices' design and control are reviewed.

Results Significant progress in integrating force feedback has been made. This has been achieved using control algorithms that improve the system's transparency and stability. Force sensors or estimation techniques are used to quantify the tool-tissue interaction.

Conclusion Commercial telesurgical systems with force feedback should be available in the near future. It is expected that the development of new robotic manipulators and bilateral control schemes continues, giving assistance to a wider spectrum of medical procedures.

Keywords: Robotic Surgery, Haptic Feedback, Master-Slave Systems, Teleoperation

Glossary

Telepresence	Impression of being present at a remote location.
Teleoperation	Operation of a machine at a distance.
Transparency	Level of telepresence achieved by a teleoperated system.
Impedance	Measure of opposition to motion of a structure subjected to a force.
DOF	Degrees of freedom.
MRI	Magnetic resonance imaging.
MIS	Minimally invasive surgery.
Haptic	Refers to all touch and touch-related capabilities .
RF	Radio frequency.
AR	Augmented reality.
ch	Channel

1. Introduction

Robotic teleoperated systems enhance the surgeon capabilities, providing high positioning accuracy, dexterity, repeatability and stability [**1**, **2**]. As can be observed in figure 1.1, a telesurgical system with force feedback capability consists of a human operator (surgeon), a master device, a communication channel, a bilateral controller, a slave manipulator and a remote environment (patient) [**3**]. The master device captures the surgeon's movement commands. The bilateral controller implements a particular interaction scheme between the master and slave devices, exchanging position, orientation and force information through the communication channels. Note that a significant time delay in the communications may be introduced by the communication channel. The slave manipulator executes the surgeon's commands, and its attached force sensor sends information about the contact force that result from its interaction with the remote environment. This force is reflected to the surgeon through the master console.

The daVinci Surgical System (Intuitive Surgical, Inc., Sunnyvale, USA) is the most used robotic telesurgical platform on the market, which is designed to perform minimally invasive surgeries. With four robotic arms the daVinci is able to manipulate three surgical instruments and an endoscope, implementing features such as motion miniaturization and tremor filtering. The surgical instruments, called EndoWrist (also provided by Intuitive Surgical), offer high manipulability, providing 7-DOF each. A dual-channel endoscope is used to obtain high-quality stereoscopic vision, allowing a better spatial orientation for the surgeon [**4**]. The main drawbacks of the daVinci are:

(1) Elevated system and instrument's costs [**5**].
(2) Bulky system's size.

(3) The absence of algorithms to avoid collisions among its arms.
(4) The lack of haptic feedback for soft-tissue interactions [**1**].

Although high-quality visual feedback is provided by telesurgical systems such as the daVinci, providing feedback for other senses, such as the touch, is challenging and there are currently no commercial systems that implement this feature [**6**, **7**].

Haptic perception involves tactile and kinesthetic (force) information [**8**]. This information is critical to successfully perform many medical procedures, such as tissue palpation and tumor localization, needle insertion, suture quality verification and tying, among others [**9**,**10**]. Furthermore, the lack of haptic feedback can lead to tissue damage, which comprises the patient safety [**3**]. Results of experimental medical tasks with teleoperated systems report a high reduction in the magnitude of peak and average forces that are exerted by the surgeon when force feedback is available [**10**–**12**].

Haptic feedback is also necessary to achieve telepresence, so the operator can perform a series of tasks in a comfortable and intuitive way, feeling present at the remote environment. Telepresence is the ultimate goal of telerobotic systems and requires to provide feedback for all human senses, while keeping all human motion abilities enabled [**13**]. The performance of a telerobotic system is measured by its transparency, which refers to the level of telepresence achieved by the system [**14**]. For bilateral-teleoperated systems transparency depends on how accurately the interaction force, between the slave device and the environment, is being reflected to the human operator through the master device [**14**]. Impedance tracking between the master and slave systems constitutes the goal of transparent bilateral teleoperation systems [**15**].

This paper reviews the recent advances in force feedback-enabled teleoperated systems for several interventional medical procedures. Active research is being mainly focused on contact force measurement/estimation, bilateral control schemes and master and slave devices design. A brief introduction to the challenges involved in each of these fields is presented next.

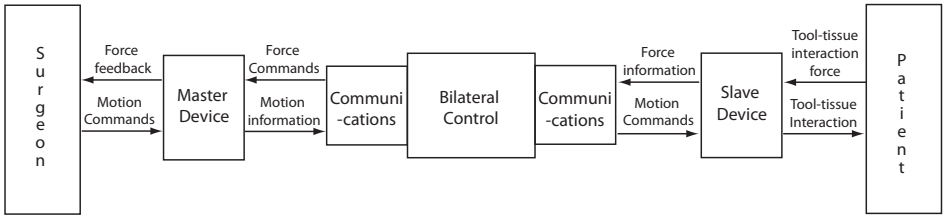

FIGURE 1.1. General scheme of a telesurgical system with force feedback.

1.1. Haptic devices. Haptic devices are used in telesurgical systems to allow the surgeon to command the maneuvers of the slave manipulators using his hands. These mechatronic interfaces are able to exert forces to the surgeon hands, which enables a bilateral exchange of information during the operation of the telerobotic system. This is achieved with the integration of sensors to measure the position of its joints and actuators that allow them to provide force feedback in several DOF. Note that from the point of view of its mechanical design, it is challenging to offer an accurate force reflection and a comfortable operation (ergonomy). Friction, inertia and backlash affect directly the quality and accuracy of force reflection; they must be kept as low as possible to ensure a proper performance [**9**]. The quality of the force reflection also depends on the performance of the device's controller. The controller design is complex because a fast response and a stable behavior are needed simultaneously. Salisbury et al. in [**16**] provides a deep discussion of the concepts and challenges involved in haptic rendering, while some of the basics are presented here.

The force feedback that is provided to the surgeon through the haptic device can include, in addition to information of real interactions (e.g. tool-tissue contact force), computer-generated forces. These virtual forces, also known as virtual fixtures, help to improve the operation of telerobotic

systems providing different modalities of force feedback [**17**]. Virtual fixtures can be classified as Guidance Virtual Fixtures (GVF) or Forbidden-Region Virtual Fixtures (FRVF) [**7**]. GVF help the surgeon to perform a movement along a defined path, while FRVF prevent the surgeon accessing a specific region of interest [**18**].

Figure 1.2 shows the simulation of a telerobotic system in which the surgeon commands the movements of a virtual robot through a haptic device. This application shows an example of a FRVF implementation, which acts like a wall in the world's XZ plane, limiting the surgeon's workspace along the world's Y-axis. An avatar is used in the virtual environment to represent the haptic device, whose geometry, in this case, corresponds to the tool that is manipulated by the slave robot. In this commanding scheme the robot controller sets the position of its joints such that its end-effector matches the position and orientation of the haptic device's avatar. For the haptic rendering of the objects that act as FRVF a collision-detection and a force-response algorithm are needed [**16**], which are briefly described next.

(1) Collision-detection: This algorithm detects if collisions between the avatar and other objects of the virtual scene take place. Examples of widely used techniques to perform this task are bounding volume hierarchies and spatial partitioning approaches [**19**].
(2) Force-response: Once a collision is detected this algorithm calculates the force that results from the interaction of the avatar and the collided object. Currently rigid and compliant interactions can be computed and additionally surface properties, such as texture and friction, are recreated in the pursuit to improve realism. Note that the complexity of calculation increases as more DOF are considered in the avatar-object interaction. For example, the result of a 3-DOF interaction corresponds to a force with three components, while a 6-DOF interaction includes additionally three components of torque [**16**].

Summarizing, in the FRVF implementation a contact force will be calculated and delivered to the surgeon when the haptic device's avatar touches the virtual fixture. In this way, neither the haptic device's stylus nor the robot's end-effector can move beyond the virtual wall. Figure 2(b) shows the position of the robot's end-effector while figure 2(c) displays the X, Y and Z components of the force that was transmitted to the surgeon. The development presented in [**7**] by Yamamoto et al. is an interesting approach that demonstrates how AR and virtual fixtures can improve telesurgical platforms. In their research AR is complemented by displaying material properties of the organs and FRVF are used to encapsulate anatomical structures, avoiding the direct contact with them.

Commercial haptic devices such as Omega and Sigma (Force Dimension, Nyon, Switzerland) (see [**20**,**21**]), PHAMTOM (SensAble Technologies, Inc., Woburn, USA) (see [**6**,**22**–**24**]) and Novint Falcon (Novint Technologies, Inc., Albuquerque, USA) (see [**25**]) have been widely implemented in various non-commercial medical telerobotic systems. However, several researchers have developed custom devices, providing consoles with a similar appearance to surgical instruments and able to measure position/orientation and reflect forces in the DOF that are available in a particular procedure (see [**9**, **26**]). Other authors have developed devices that have similar kinematics to the slave manipulators, so they are able to command the movement of the slave manipulator's joints individually (see [**27**, **28**]). Figure 1.3 shows an example of a custom device for endoscopic surgery and a commercial haptic device used in telesurgical applications.

1.2. Force measurement and estimation. One of the main challenges in providing force feedback is the measurement of the contact force of the robot's end-effector with the patient's tissue. Space constraints, sterility requirements, proper placement of the sensing element and costs are the main aspects to assess when integrating force/torque sensors to surgical instruments (slave robot's tool) [**29**].

For MIS procedures the fulfillment of these requirements is particularly difficult due to the nature of these techniques. Puangmali et al. in [**30**] discuss the design considerations of installing force and tactile sensors to MIS surgical instruments, introducing also a review of the recent advances in sensing technologies and methods. Figure 1.4 shows a sensorized surgical instrument developed by the German Aerospace Center (DLR).

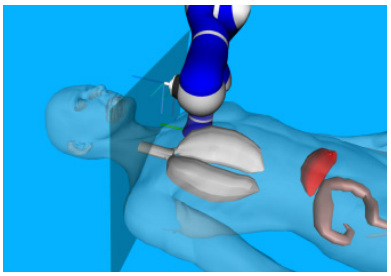

(a) Interaction of a simulated robot with a FRVR. Courtesy of Vicomtech-IK4 eHealth and Biomedical application laboratory.

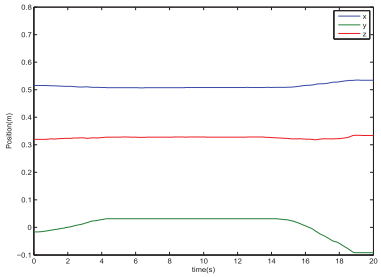

(b) Graphic representation of a simulated KUKA LWR robot and a FRVF in the XZ plane.

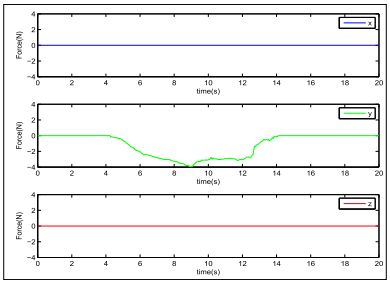

(c) Robot's end-effector position vs. time.

FIGURE 1.2. Interaction of a simulated robot with a virtual fixture. Courtesy of Vicomtech-IK4, eHealth and Biomedical applications lab.

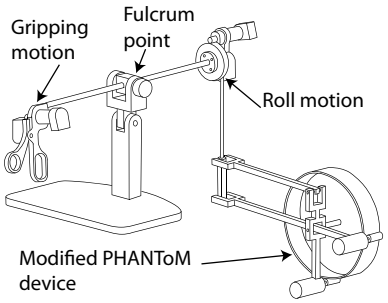

(a) Schematic diagram of the haptic interface developed by Tavakoli et al. in [**9**].

(b) Omega6 haptic device from Force Dimension.

FIGURE 1.3. Custom and commercial master devices used in telesurgical systems.

Other authors have implemented methods to estimate the tool-tissue interaction force, avoiding the installation of force sensors. Examples of this approach can be found in references [**31**–**33**], which implement different observers to estimate the aforementioned force. Also references [**3**, **34**] use a function parameter matrix and a recursive least-squares method to perform the force estimation. Note that the accuracy of the estimation is strongly influenced by the quality of the model of the manipulator.

In the implementation of certain bilateral teleoperation schemes the interaction force between the operator's hand and the haptic device is required. Since most of the commercial haptic devices are not equipped with force sensors, this force needs to be estimated. Talasaz et al. [**35**] estimate the hand-master device interaction force through the implementation of a force observer.

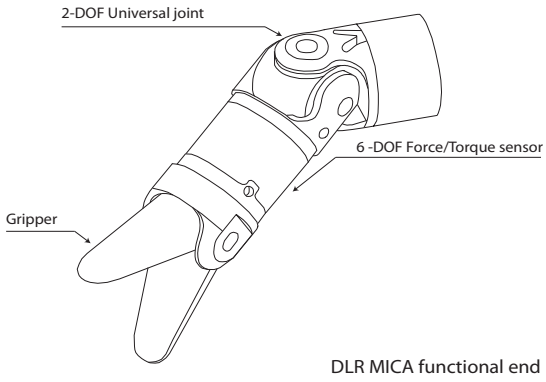

FIGURE 1.4. Schematic diagram of a DRL surgical instrument equipped with a six-axis force-torque sensor [**30**].

1.3. Bilateral control strategies. In many medical applications, unilateral control schemes that are only based on position tracking between the master and slave devices do not ensure the procedure to be successful and safe. The integration of force information in the control loop helps to improve the procedure's safety, as large forces can be avoided and unexpected objects can be detected [**29**]. The 3ch control arquitecture presented by [**14**], acceleration based control schemes implemented by references [**15**, **31**, **33**, **36**] and the hybrid impedance control introduced by [**35**] are some of the recent advances in bilateral control, outperforming previous schemes such as position-position and force-position. Figure 1.5 shows the force-position approach that was assessed by Talasaz et al. in [**35**]. For this scheme F_h and F_e are the hand/master and slave/environment interaction forces. Z_h, Z_e, Z_m and Z_s correspond to the operator's hand, environment, master console and slave manipulator impedances, representing the dynamic characteristics of each one of these systems. The position of the master and slave devices are denoted by X_m and X_s. $\tilde{F}_h$ and $\tilde{F}_e$ represent the exogenous input forces exerted by the operator and remote environment, respectively, which are independent of the system response. C_s is the local proportional-derivative position control of the slave robot.

Ideally, bilateral control algorithms should provide high transparency and stability. However, it is difficult to achieve both goals simultaneously. Improving transparency while preserving stability requires to eliminate the uncertainties of the model and the exact implementation of the control laws [**14**, **33**]. The complexity of achieving a proper behavior is increased when time delay in the communication among the different components of the system is present. Several approaches have been proposed to tackle this problem; most of them are based on the passivity framework [**13**, **15**], in which stability is guaranteed if each component of the system behaves passive (do not increase the system's energy) [**21**, **37**]. Zhu et al. in [**37**] provide a survey of the main control approaches for bilateral teleoperation with time delay, reviewing the advantages and weaknesses of passivity based, prediction based and sliding-mode control schemes. One of the new efforts to improve the system operation performance, under time delay, is presented by Ohnishi et al. [**15**], which introduce a time delay compensator based on network disturbance. In opposition to other compensators for variable time delay, this one does not require the derivation of a time delay model.

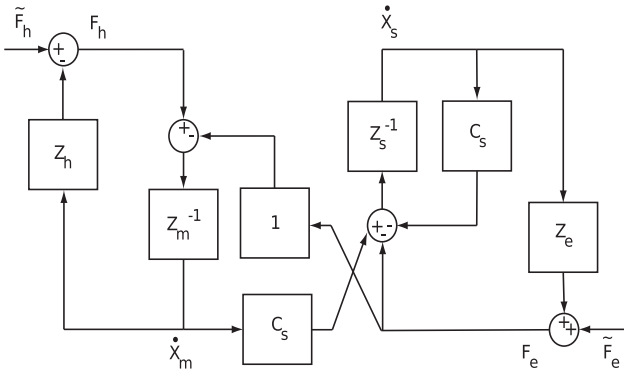

FIGURE 1.5. Force-position bilateral control scheme assessed by Tavakoli et al. in [**14**].

Other interesting approaches to provide a safer use of teleoperation systems are presented by references [**38**] and [**36**]. Gaparetto et al. in [**38**] propose a control strategy that reflects forces to the surgeon only when this one is grasping the master device. This contributes to maintain the system's stability and the patient's safety, as undesired movement commands are avoided. Kasahara et al. in [**36**] present a method for detecting the rupture of tissue in exenteration procedures. The proposed method estimates the environmental impedance online using a reaction force observer and a recursive least squares algorithm. A drastic change in the environment's stiffness indicates the rupture occurrence, which is identified by the proposed algorithm, and therefore, allows the opportune identification of accidents. Figure 1.6 illustrates the acceleration-based control scheme implemented in this application. X_m^{res} and X_s^{res} correspond to the position response of the master and slave devices. The estimated force response values for the master and slave robots are denoted by f_m^{res} and f_s^{res}. The acceleration references produced by the controller are $\ddot{X}_m^{res}$ and $\ddot{X}_s^{res}$, for the master and slave devices respectively. M_n is the nominal mass of the master and slave systems. C_p and C_f represent position and force controllers. Note that the master and slave blocks include a disturbance observer (DOB) and a reaction force observer (RFOB).

1.4. Slave robots. Current surgical manipulators can be classified as specialized or versatile devices. Versatile devices are designed to be able to perform several interventional procedures, allowing a flexible setup and various control modes [**39**]. Most of the versatile robots are based on the design of industrial manipulators, with one or several redundant joints, providing great positioning flexibility. Recently a new generation of compact and lightweight robots has been developed. They are specially equipped with torque sensors to enable a compliant behavior, increasing the operating room (OR) staff and patient safety. Examples of these robots are the KUKA LWR IV (KUKA Roboter GmbH, Augsburg, Germany) [**40**] (see 1.7) and DLR MIRO [**39**]. The implemented control modes include, besides the typical position control, cartesian and axis-specific impedance schemes. Impedance control enables the robot to act like a spring-damper system with adjustable stiffness and damping parameters. This flexible compliance configuration allows the implementation of a gravity compensation mode (also known as hands-on mode) in which the operator moves the robot freely with his hands, as a joint-level torque controller sustains the weight of the robot. A practical application of the gravity compensation mode is presented in reference [**41**], where it is used to ease the trajectory planning of a laser osteotomy system.

The nature of some procedures imposes constraints that have led to the development of custom and specialized manipulators. MRI-compatible manipulators are restricted to be built without using ferro-magnetic and electrically conductive materials because they produce artifacts in the obtained images [**22**, **42**]. Drives, power transmission, position and force sensors must be carefully designed and chosen to avoid perturbing the magnetic field, while guarantying proper functionality. Other

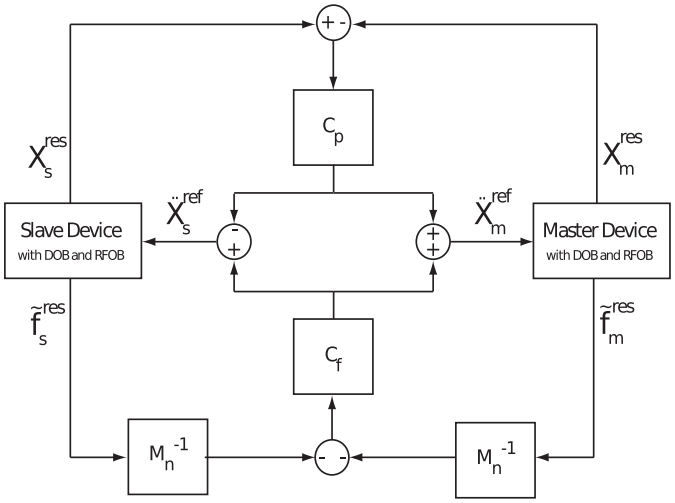

FIGURE 1.6. 4ch bilateral control system based on robust acceleration control used by Kasahara et al. in [**36**].

examples of specialized devices are the robots designed for Natural Orifice Transluminal Endoscopic Surgery (NOTES). For this procedure the slave manipulator should be flexible and narrow, as it is to be introduced with a flexible endoscope via natural orifices [**27**]. Phee et al. in [**27**] implemented a tendon-sheath actuation mechanism to accomplish these requirements.

FIGURE 1.7. KUKA LWR IV+ lightweight robot embedded to a surgical bed. Courtesy of Vicomtech-IK4, eHealth and Biomedical applications lab.

2. Taxonomy

In this paper the conducted taxonomy presents the recent developed teleoperated mechatronic systems, with force feedback, clustered according to the medical procedure they were designed for.

2.1. Endoscopic surgery. The endoscopic and laparoscopic procedures offer several benefits to patients such as less trauma, smaller scars and shorter recovery times [**11**]. However, these procedures impose great complexity to surgeons because a reduction in the depth perception, dexterity and haptic feedback take place [**10**]. Robot-assisted MIS has led to overcome most of the procedure's problems, improving dexterity and safety [**43**–**45**]. Several developments have been performed to provide force feedback-capable teleoperation systems for these procedures; a brief review of them is presented next.

Tanaka et al. in [**31**] continue their previous work reported in [**46**], in which Field Programmable Gate Array (FPGA) chips constitute the core of the hardware used for bilateral control implementation. The use of FPGA chips allows small sampling periods. In particular, the authors report a sampling period around $30\mu s$. This fact is decisive in the performance of the implemented bilateral control strategy, which is based on acceleration control and requires sampling periods as short as possible. The idea behind this strategy is to achieve position and force control through the control of a variable that is common to them: acceleration. In this control strategy the interaction force of the surgical instrument (forceps) with the environment is estimated using a force observer. The control algorithm is implemented using four FPGA chips. In reference [**31**] redesigned 7-DOF master and slave devices that solve the mechanical malfunctions of their previous designs are also presented.

Weede et al. in [**20**] enhance the robotic platform developed by Mönnich et al. in [**41**] for MIS teleoperation tasks.. The system developed at the Karlsruhe Institute of Technology (KIT) is composed by three industrial robots; two of them for surgical instrument manipulation (KUKA LWR IV) and the third (Stäubli RX90) handles an endoscopic camera (see figure 1.8). The KUKA robots are commanded through two haptic devices, delta6 and Omega7, as can be observed in figure 1.9. The instrument-tissue interaction force estimation is possible due to the integrated force sensors of the KUKA LWR robot. The system is able to align the endoscopic camera with the instruments' tips using information extracted from previous surgeries. The control algorithms are implemented using Simulink (The MathWorks, Inc., Natick, USA) and Real-time CORBA, which allows performing the data exchange among the different systems.

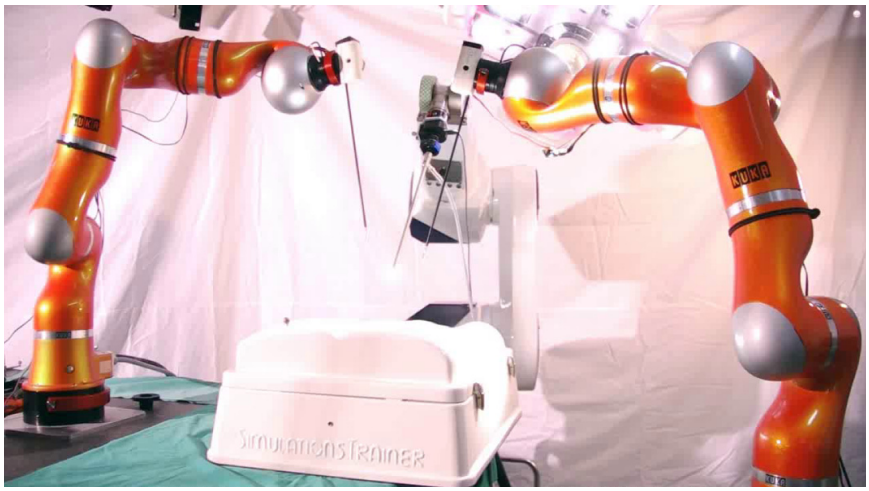

FIGURE 1.8. KIT Robotic prototype set-up for MIS implemented by Weede et al. in [**20**]. Courtesy of the Karlsruhe Institute of Technology.

Beyl et al. in [**47**] extended the platform presented by [**20**] with the integration of virtual fixtures to the haptic rendering. Here FRVF are used to represent organs or virtual geometrical constraints, limiting the surgeon's workspace. The surgeon has the possibility to create the desired FRVF in the same imaging framework in which the patient's medical images are displayed. The haptic rendering

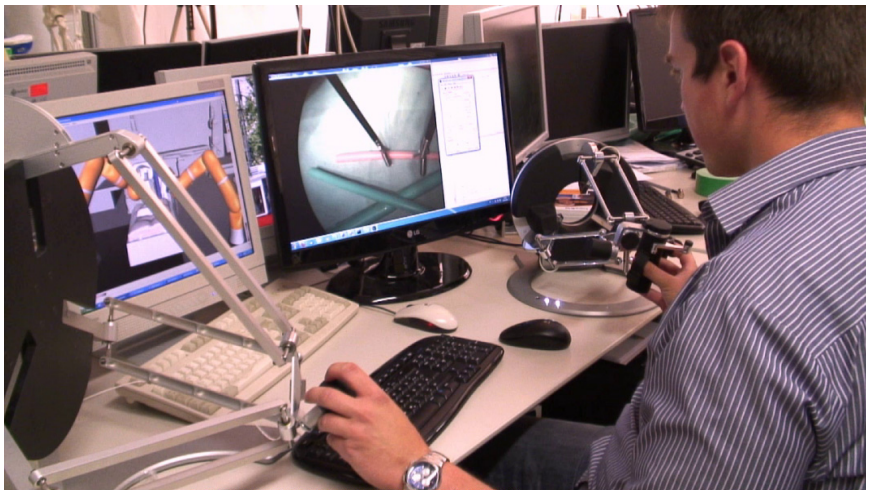

FIGURE 1.9. Graphic user interface and haptic devices of the KIT surgical platform [**20**]. Courtesy of the Karlsruhe Institute of Technology.

of the virtual fixtures is performed with the C++ open source CHAI3D API. The combination of real and virtual interaction forces enrich the haptic perception of the surgeon, preventing him accessing a critical region or avoiding undesired interactions with surrounding organs during the surgical procedure. The authors also discuss the necessity of informing the surgeon if the current force feedback comes from a real or a virtual interaction. To achieve this, they superpose a slight vibration to the forces that result from contact with virtual fixtures.

Hagn et al. in [**21**] present MiroSurge, a particular configuration of the MIRO Robotic Surgery Platforms (MRSP). This setup is meant to perform bimanual endoscopic telesurgery, offering the possibility to implement different robotic configurations, control and interaction modes. The slave devices are DRL MIRO robots (see [**39**]), while two Omega7 haptic devices are used as master consoles. The instruments are equipped with force sensors that allow to obtain measurements in 7-DOF. The proposed control strategy is based on a hierarchical layer architecture, allowing bilateral teleoperation (force-position scheme) with multi-arm coordination, enabling collision avoidance among the robots (see [**48**]). The control algorithms are designed using Matlab/Simulink and C/C++ code is obtained using the Matlab's Real-Time Workshop. Six computers with QNX Neutrino real-time operating system (OS) (QNX, Ottawa, Canada) run the compiled code, implementing a distributed control system using the aRDnet-suite (see [**49**]). Figure 1.10 illustrates the MRSP robotic setup.

2.1.1. *NOTES.* A special case of endoscopic surgery is the Natural Orifice Transluminal Endoscopic Surgery (NOTES). In this surgical procedure the access to the abdominal cavity is preformed through transvaginal, transgastric, transvesical or transcolonic routes [**50**]. Phee et al. in [**51**] proposed the Master And Slave Transluminal Endoscopic Robot (MASTER), which is a device suited for NOTES and Endoscopic Submucosal Dissection (ESD). The MASTER is a 7-DOF robot with a power transmission system that consists of a tendon sheath mechanism. This allows the robot to be flexible and small, as all the actuators are located outside the manipulator. Initially the MASTER system did not provide haptic feedback. In order to add force feedback capability to the system, Yang et al. in [**52**] developed a method to estimate the force at the robot's end-effector. Through the formulation of a mathematical model of the transmission system, the interaction force of the tool is estimated based on the force measurements at the proximal ends of the sheaths. For this purpose two load cells were installed for each DOF actuated by two tendon and sheaths. Later, Sun et al. in [**28**] proposed some improvements to the system introduced by [**52**]. They developed a modified force transmission model, allowing the computation of more accurate force estimations. Also, the

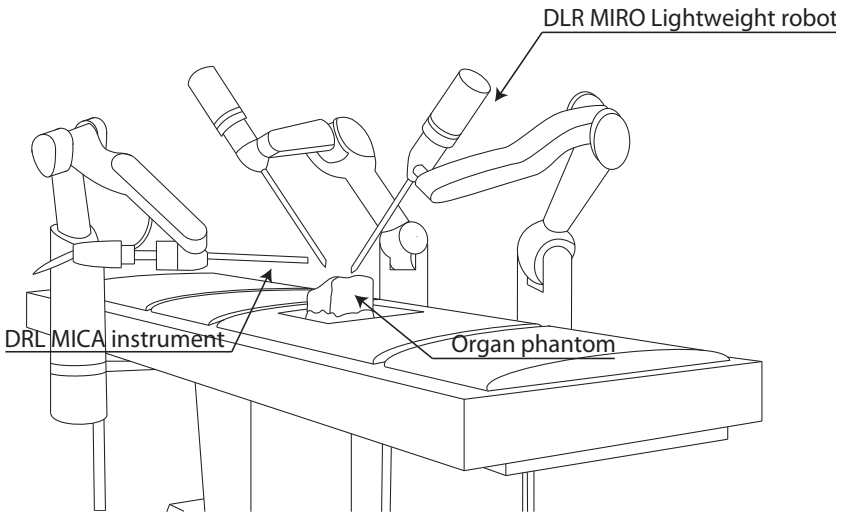

FIGURE 1.10. Schematic diagram of the DLR MiroSurge robotic system presented by Hagn et al. in reference [**21**].

master console was equipped to be able to provide force feedback and it was redesigned to match the slave device's DOF, allowing the surgeon to command the movements of each joint of the slave robot individually (see figure 1.11). This commanding scheme differs from the one presented by references [**20**, **21**, **35**], which use the position and orientation of the haptic device's stylus as the position and orientation set-points of the slave robot's tool. Note that to achieve these position and orientation references it is necessary to calculate the slave robot's inverse kinematics, obtaining the proper angles for its joints.

2.1.2. *Palpation for abnormal tissue localization.* The detection of abnormal anatomical structures through palpation helps the surgeon to localize and establish the boundaries between unhealthy and healthy tissue during surgical procedures. This task is difficult during traditional MIS due to the restricted dexterity and reduced haptic feedback [**10**, **53**]. Robotic telesurgery can help to overcome these shortcomings by increasing the manipulability of the instruments and reestablishing the haptic perception.

Mahvash et al. in [**32**] used a custom version of the daVinci surgical system for palpation experiments. The system is controlled through the implementation of a position-position control scheme with inertia and friction compensators, which improve the system's transparency. A state observer is used to estimate the interaction forces with the environment, providing force feedback without the installation of force sensors on the slave device. Several tests were performed to evaluate the impact of direct and graphical force feedback modalities; they consisted in localizing stiff objects placed inside heart and prostate models. Results with the heart model indicated that direct force feedback improved the localization accuracy in comparison with no force or graphical feedback modalities. However, outcomes with the prostate model showed no benefit from using direct or graphical force feedback. Authors suggested that the use of tactile sensors and display could be more helpful in the latter case given the small change in the stiffness between healthy and unhealthy tissue in the prostate.

Trejos et al. in [**53**] present the development of a tactile sensing instrument (TSI) to obtain pressure distributions during palpation using a commercial PPS TactArray sensor (Pressure Profile Systems, Inc., Los Angeles, USA). Tumor localization experiments using phantoms were carried out to evaluate the performance of the TSI, when used manually and also with a robot. Experimental

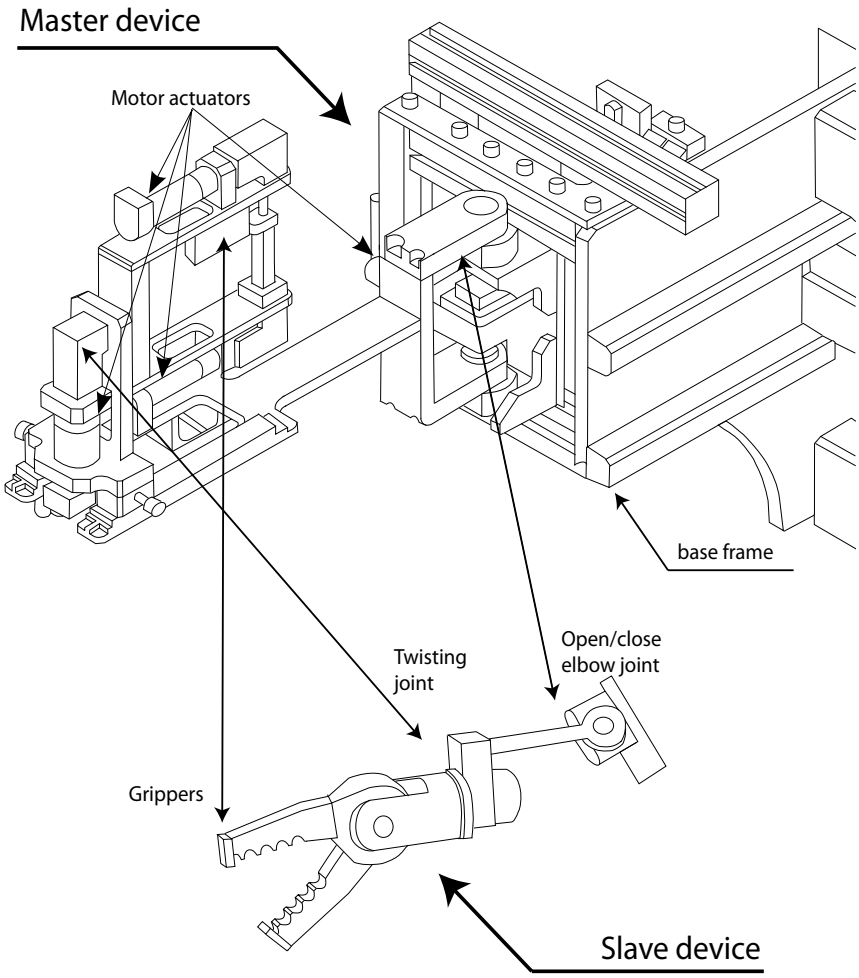

FIGURE 1.11. Schematic diagram of the Master and slave devices designed by Sun et al. in [**30**] for NOTES.

results showed that the success of the tumor localization greatly depends on the uniformity of the applied force during exploration.

In accordance with the mentioned conclusions, Talasaz et al. in [**35**] present a teleoperated system that combines force and tactile feedback for tumor localization. The pressure distribution obtained from the tactile feedback is shown to the surgeon as a color contour map, while interaction forces are reflected to his hand through a haptic device. This data fusion allows the surgeon to control the exploration force, improving the tumor identification and localization tasks. The teleoperation system consists of 7-DOF master and slave devices. The master console is a modified Quanser Haptic Wand (Quanser, Inc., Markham, Canada), while the slave manipulator is a Mitsubishi PA10-7C robot (Mitsubishi Electric Automation, Inc., Vernon Hills, USA). The TSI presented in [**53**] is used to obtain the tactile data and a 6-DOF ATI Gamma force/torque sensor (ATI Industrial Automation, Inc., Apex, USA), installed at the robot's wrist, is used to measure the force that results from the robot's end-effector and environment interaction. The implementation of a hybrid impedance control for both the master and slave devices allow a proper performance of the system when the slave

manipulator is in contact with tissue. This controller generates acceleration references to control both position and force. The interaction force between the surgeon's hand and the haptic device is required for the aforementioned bilateral control implementation. Since no force sensor is installed on the master device, this data is estimated through a force observer. Simulink was used to design the control algorithms, and real-time code was obtained using the QuaRc software (also produced by Quanser).

2.2. Catheterization and Needle insertion. Radio frequency catheter ablation is one of the medical procedures to threat arrhythmia. It is traditionally performed manually by the surgeon under extensive X-ray exposure for himself and for the patient [**54**]. Teleoperated systems are being developed for this procedure in order to improve the catheter positioning and reduce the procedure time; thus, decreasing the exposure period to X-ray [**55**]. In the pursuit to provide a haptic-enabled teleoperated catheter navigation system, Park et al. in [**54**] present a prototype with custom master and slave devices. The slave manipulator allows 1-DOF of translation (forward-backward motion), 1-DOF of rotation (turn around the translation axis) and 1-DOF for the catheter tip bending. It has installed a load cell to measure the interaction force along the catheter translational axis, while force in the roll joint is estimated from the motor current consumption. The master console is designed to command the movements of the slave joints individually and is equipped with actuators to provide force feedback. Joint-level proportional-integral-derivative (PID) controllers are used to achieve position control in the slave manipulator and force control in the master device. Control algorithms are programmed in C and run on a PC under RTLinux-Pro real-time OS (Diamond Systems, Mountain View, USA).

Other medical procedures based on needle insertion require continuous MRI. As mentioned in section 1.4, providing telerobotic systems with MRI compatibility is a complex task because its mechatronic design has to fulfill several constraints. The slave manipulator must be compact to fit in the limited space of the scanner bore. For its mechanical structure, the use of high strength plastics, carbon fiber, advanced ceramics and no ferrous metals is necessary to avoid magnetic perturbations [**22**, **25**]. Also, the selection and design of drives and motion transmission systems is challenging because friction and backlash have to be minimized to achieve a proper positioning. In accordance with this guideline, long transmission systems must be avoided and alternative motion drives (e.g. hydraulic and pneumatic actuators) are considered [**22**].

Advances in providing haptic feedback for these MRI-compatible systems have been reported recently. Su et al. in [**25**] present the design of a teleoperation system for prostate brachytherapy. The master console is a commercial 3-DOF Novint Falcon, while the custom slave device is composed of a 3-DOF linear platform and a 3-DOF needle driver. A 3-DOF fiber optic force sensor is installed in the needle driver, allowing the measurement of the needle insertion force. Piezoelectric linear and rotary motors are used to provide motion of the linear and needle driver stages of the slave manipulator. These piezoelectric actuators provide several benefits such as a high holding force when unpowered and the possibility to implement cascade configurations to increase output force along a desired motion axis. However, commercial hardware for their motion control is expensive. Figure 1.12 illustrates the developed slave device.

Kokes et al. in [**22**] present a MRI-compatible teleoperated system prototype for radio frequency ablation (RFA) of breast tumors. The system implements a commercial PHANTOM haptic device as the master console and a 1-DOF needle driver as the slave manipulator. With the use of a hydraulic cylinder the needle driver allows the movement along the needle longitudinal axis. Its position is measured with an optical linear encoder and the velocity of the actuator can be regulated due to integration of proportional electrovalves in the hydraulic circuit. A 6-DOF strain gage is installed to measure the interaction forces/torques of the RFA tool. However, only the force along the translational axis of the needle driver is forwarded to the haptic device. A PI control scheme is implemented to perform the position control of the actuator with a 1 kHz sampling frequency. Experimental results showed a good performance of the position control, while the force feedback allowed the operator to distinguish between healthy and unhealthy tissue. Although the implemented force sensor was modified to be MRI-compatible, the magnetic field induced high noise to the measurements in the

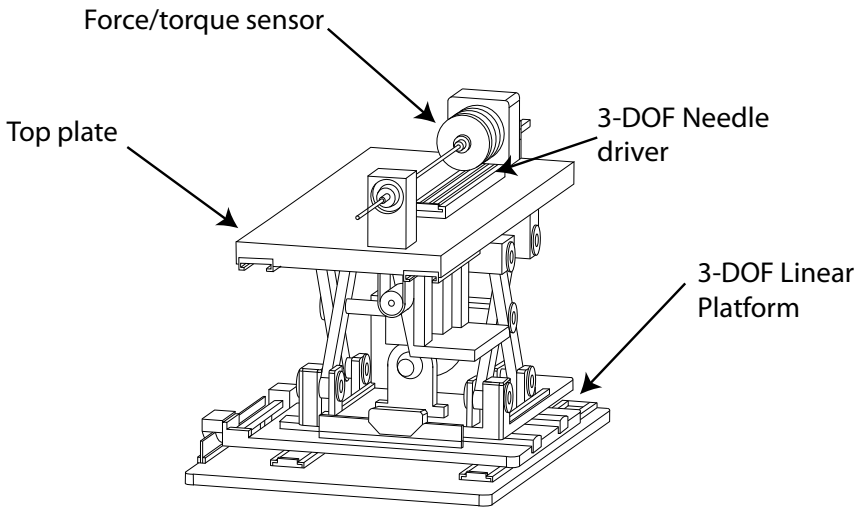

FIGURE 1.12. Schematic diagram of the MRI-compatible slave robot developed by [**25**]. The device consists of a 3-DOF linear stage, force sensor and a 3-DOF needle driver.

force components that are orthogonal to the insertion axis. One of the proposed alternatives to solve this problem is the use of optical sensing methods.

2.3. Microsurgery. Microsurgical procedures address the intervention of tiny anatomical structures. This technique is applied in several medical specialties such as otolaryngology, ophthalmology, urology, gynecology, neurology and reconstructive plastic surgery among others [**56**]. These procedures are typically performed manually by the surgeon, which obtains visual feedback using a microscope and manipulates special instruments. Robot-assisted microsurgery extends the surgeon's abilities, achieving precise positioning and tremor-free maneuvers, allowing to perform tasks at sub-millimeter scale [**57**].

Lang et al. in [**58**] introduce the neuroArm. This system is developed by the University of Calgary since 2002, and it is designed to perform neuro-surgical procedures. With two arms of 7-DOF each, which receive the movement commands through two master devices, this robot is able to perform microsurgical interventions. The neuroArm is built to be MR-compatible, which is achieved using titanium and polyetheretherketone for the structure and piezoelectric motors for the motion system. The manipulators have installed six-axis force/torque sensors for measuring the contact force exerted by the surgical instruments. The information obtained from the force sensors is used to provide force feedback (in tree translational DOF) to the surgeon, visually and also through the master consoles. The surgeon can obtain a rich visual feedback accessing to different information sources through several displays, including MR-images obtained during the surgery and stereoscopic video from the microscope. A remarkable achievement of this system is that it has been successfully used in surgical procedures with humans.

3. Conclusions

Important advances have been achieved in medical experimental teleoperation platforms. In addition to providing force feedback, functionalities such as multi-arm coordination, automatic endoscopic camera positioning, virtual fixtures rendering and visual feedback augmentation are being developed by several research groups around the world. These features, which are not available in current commercial telesurgical systems, allow performing a safer intervention, helping the surgeon to focus on the procedure without worrying about the operation of the system.

Although recent efforts in providing haptic telesurgical systems mainly implement industrial-type manipulators, new slave devices are being designed to cover the requirements of other procedures such as NOTES and interventions that require continuous MRI. This enhances the spectrum of interventions that can be improved with the assistance of robotic manipulators. Also, the development of lightweight robots with built-in torque sensors has allowed the implementation of new interaction modes and control schemes (e.g. hands-on mode and impedance control), which greatly contribute to make the interaction between robots and humans safer and easier.

Extensive efforts have been invested to integrate force/torque sensors to surgical instruments. Strain gages are commonly used for most of the applications, while new sensing technologies, such as optical methods, are being explored to provide MRI-compatible devices. Despite of the advances in force sensing, the use of force observers to estimate the interaction forces in teleoperated systems is still common. This fact is mainly caused by the costs involved in the development of technologies for clinical use.

In the field of bilateral control, new schemes are being introduced to cope with the adverse effects produced by the presence of time delay in the communications of teleoperated systems. Most of the proposed strategies to tackle this problem are based on the concept of passivity to perform the controller design and stability analysis. The development of control theory around this topic is necessary, as the possibility of executing surgeries where the surgeon and patient are separated by hundreds of kilometers is to be exploited, and therefore time delay in the communication channel is significant.

Conflict of interest. None declared.

CHAPTER 2

A New Evaluation Framework and Image Dataset for Key Point Extraction and Feature Descriptor Matching

CONTEXT: A project to obtain an image dataset and devise an evaluation framework to establish an assessment methodology for keypoint extraction and feature descriptor matching algorithms, based on normalized data and protocols, was developed at VICOMTech institute. The mentioned algorithms play a key role in several domains, such as 3D reconstruction, object recognition, camera tracking and augmented reality. All of these applications have been extensively integrated in interventional and diagnostic medical procedures and systems.

This work has been founded by Universidad EAFIT, the Colombian Council of Research and Technology (COLCIENCIAS) and VICOMTech Institute. Camilo Cortes, research assistant under my direction in the CAD CAM CAE Laboratory, was able to program the application of the devised methods. The contributions of this work have been submmited to The International Conference on Computer Vision Theory and Applications (VISAP 2013) and are pending for publication.

- Iñigo Barandiaran[1]
- Camilo Cortes[1,2]
- Marcos Nieto[1]
- Manuel Graña[3]
- Oscar E. Ruiz[2]

[1] eHealth and Biomedical Applications, VICOMTech-IK4
Mikeletegi Pasealekua 57, San Sebastián, Spain
[2] CAD CAM CAE laboratory, Universidad EAFIT
Carrera 49 No 7 Sur - 50, Medellín, Colombia
[3] CCIA Department, UPV/EHU
San Sebastián, Spain

As co-authors of such publication, we give our permission for this material to appear in this document. We are ready to provide any additional information on the subject, as needed.

Prof. Dr. Eng. Oscar E. Ruiz
oruiz@eafit.edu.co
Coordinator CAD CAM CAE Laboratory
EAFIT University, Medellin, COLOMBIA

ABSTRACT. Key point extraction and description mechanisms play a crucial role for image matching, where several image points must be accurately identified to robustly estimate a transformation or recognize an object or a scene. Currently several new mechanisms for key point extraction and for feature description are emerging, so normalized data and evaluation protocols are needed in order to assess them accurately. In response to these needs, we present a new evaluation framework for measuring different aspects and behaviours of the state-of-the-art feature point extraction and description mechanisms. In addition, we also propose a new image dataset and a testing image generator. This evaluation framework and dataset can be useful to help the research community improving their key point extraction and feature descriptor approaches. Also, the practitioners on computer vision applications, based on image point matching, can obtain valuable information from this contribution to select the algorithm that best suit their needs. All proposed material in this work is freely available on-line.

Keywords: Key point Extraction, Feature Descriptor, Key point Matching, Homography Estimation.

1. Introduction

Interest points extraction and matching is nowadays a common task in many computer vision based approaches, which are applied in many different domains, such as 3D reconstruction, object recognition, camera tracking and augmented reality. Key point extraction and description mechanisms play a crucial role during image matching processes, where several image points must be accurately identified to robustly estimate a transformation or recognize an object. Currently there is an increasing activity in the development of new approaches for key point extraction, description and matching, trying to get more robust and computationally lightweight approaches. In this way, we think that normalized data and evaluation protocols are needed in order to assess them accurately.

In this work, we present a new testing framework, an image dataset, and a testing image generator for the evaluation of the state-of-the-art key point extractors and feature point descriptors. This appraisal is done by measuring several algorithm features, such as repeatability, accuracy and invariance to affine transformations or photometric transformations. Our new proposed testing dataset comprises both a transformed image generator, that allows generating new images with geometric and photometric transformations, and a set of real images acquired with different types of sensors and conditions, showing also variations in both geometric (such as similarities or affinities) and photometric transformations.

The dataset of real images, the image generator with the evaluation framework form a useful tool to help in the selection of the proper algorithm to develop computer vision applications based on image point matching, and to improve or develop new approaches for key point extraction or point matching.

The paper is structured as follows: section 2 provides a brief description on key point extraction and feature descriptors and an overview of some evaluation framework and testing datasets. Section 3 describes the proposed framework for feature point descriptor evaluation. Sections 4 and 5 describe both the proposed acquired real image dataset and transformed image generatorin and finally section 6 gives final remarks and depicts the future work.

2. Related Work

Several computer vision based applications rely on the identification or matching of several discrete points extracted from the images. Although this is a very common task, depending on the nature of such applications, the requirements for a specific key point extractor and descriptor may vary. For example, applications related with self-navigation or simultaneous location and mapping (SLAM) would require a fast key point extractor algorithm because of its real-time restrictions. On the other hand, an application for object or image recognition would benefit from more robust or better invariant key point extractor; even if this implies a higher computation time. In the context of point matching, a robust key point can be understood, in general, as a point of the same structure in the

scene that is able to be extracted and matched even if some types of geometric or photometric transformations occur between different image acquisitions.

In [**59**] the authors suggest that there are several parameters of a point detector and feature descriptor that can be measured; they also cite the most relevant ones. However, measuring some of them, such as the point extractor accuracy, descriptor robustness or invariance needs a normalized test protocol and test benchmark. In this way, the seminal works of [**60**] settled the basis for key point extractor and feature description evaluations. Since then, several new approaches for key point or region extraction [**61**] and for feature descriptor [**62–65**] were tested against their dataset and evaluated with their corresponding scripts freely available online at `'www.robots.ox.ac.uk/~vgg/research/affine/index.html'`.

In [**66**] the author proposed an extension of the work of [**60**] by analyzing key point repeatability for non-planar scenes, using tri-focal tensor geometric restriction for estimating the ground-truth data of their own dataset. They found several differences in key points repeatability scores when applied to non-planar scenes. Recently, [**67**] proposed a dataset consisting of several videos of surfaces, with different types of textures and different light conditions, which are used to evaluate key point matching strategies oriented to camera tracking applications. The authors claim that due to restrictions in the hardware they used to move the camera for the generation of different points of view, they could not reproduce exactly the same movements every time they changed scene conditions. This implies that homographies are not the same and may bias the results of the different algorithms. They used 4 markers attached to each picture in order to compute image to image homographies.

Very recently, in [**68**] the authors tested their new descriptor approach with the known dataset and evaluation framework of [**69**]. However, they also tested their descriptor with a non-publicly accessible approach in `computer-vision-talks.com`, which is similar to our evaluation framework proposal. This framework allowed the authors to compare the robustness of their descriptor against different geometric transformation values, in the form of a ratio between correct and wrong matches. The authors affirm that this approach provides a very useful insight about the tested descriptors.

Our dataset and evaluation framework is based and inspired by the developments of [**60**]. In comparison to Mikolajczyk's approach, our dataset comprises a higher number of images, with higher resolution and with better controlled conditions.

We also include a set of images obtained with mobile devices. We think that it is important to consider some features of these devices, such as their low dynamic range, in a testing data. This is relevant since mobile devices are becoming part of our everyday lives and computer vision applications are increasing their popularity. To the best of our knowledge, this feature lacks in the available testing datasets.

In this way, our dataset includes a set of images that can be used to evaluate the robustness of key point extractors and descriptors approaches against photometric transformations, such as luminance and chrominance noise addition.

Finally, we also propose a transformed image generator that can be used to provide more testing images to a given key point or descriptor evaluation.

All proposed material in this work, i.e. images, code and binary executables will be freely available on-line at `'www.vicomtech.tv/KeyPoints'`.

3. Evaluation Framework

We have implemented an evaluation framework based on the one present in the Open Source Computer Vision Library (OpenCV) [**70**], derived from the original work of [**60**]. This framework uses the class hierarchy implemented in OpenCV that nicely decouples key point extraction from key point description and descriptor matching. In this way, the user can easily define experiments by mixing several point extractor with key point descriptors and matchers. Whereas Mikolajczyk's work, where the framework is written in Matlab scripting, our approach is written in C++. In the case of the mentioned Matlab-based evaluation framework, the user needs to generate both a file with detected key points in a given image, and the corresponding key points descriptors in order to evaluate

them. The generation of these files can be cumbersome in some contexts, such as development of commercial computer vision based applications, because the whole solution may not be tested in the same development platform. We think that our approach helps in the evaluation of future extractor or descriptor approaches because it can be easily integrated in a development environment, without the need to export additional data to other platforms. Nevertheless, our approach also supports the reading of Mikolajczyk file format, allowing the comparison with previous approaches or studies.

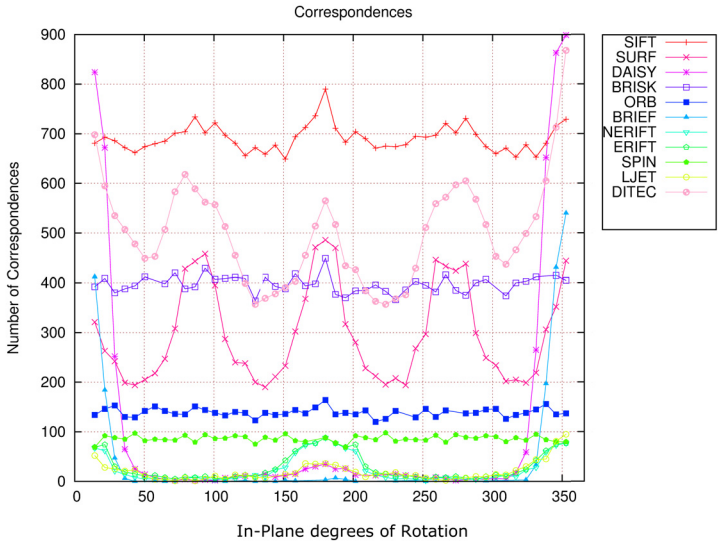

FIGURE 2.1. Results of the evaluation of several feature descriptors using the in-plane rotation.

Figure 2.1 shows partial results of an evaluation conducted using the proposed dataset and evaluation framework. In addition to the precision-recall curves proposed by [**69**], we propose to generate more informative curves about the performance of different approaches based on the number or percentage of correct matches given specific values of the evaluated transformation. For example, Figure 2.1 shows the result of the number of correct matches of several feature descriptors against a dataset composed of several in-plane rotations of an image. These preliminary results suggest that, for example, BRIEF descriptors are not robust against a rotation larger than 35 degrees approximately, or how SURF approach is more sensitive to orientations like 90, 180 and 270 degrees, possibly due to discretization effects related with the use of box filters for approximating LoG filtering. In this way, a better insight of the behaviour of a given approach may be obtained.

3.1. Matching Evaluation. An image formation process is usually represented as in Equation 1 where X_w represents world point, x_i represent world points projected in the image. P represents the projection matrix, described in Equation 2, where K describes the transformation from the camera reference frame to the image reference frame, and $[R|t]$ the composition of a translation and a rotation transformation between world and camera coordinate systems.

$$x_i = PX_w \tag{1}$$

$$P = K[R|t] \tag{2}$$

When either world points X_w lie on a world plane, or the images are acquired with a rotating camera around its center of projection, the transformation between image points x_i and world points X_w are related by a 2D linear projective transformation or homography H [**71**].

As in the dataset proposed in [**69**], in our proposed dataset all images are related by a 2D homography H_{abD}. This known transformation is used as ground truth data, allowing to know a priori where a point x_{iaD}, extracted from image a of dataset D, should be projected in image b of the same dataset, by using Equation (3).

$$x_{jbD} = H_{abD} x_{iaD} \tag{3}$$

Similarly, points extracted from image b can be projected back to image a by using the inverse of H_{abD}. Let $\tilde{x}_{jbD}$ be the estimated match of point x_{iaD} in image b obtained by the point detector algorithm. Then, the known transformation H_{abD} is used to measure the accuracy and repeatability of a point detector algorithm. This process is performed by computing the Euclidean distance d between the estimated and the ground truth points of a pair of images, as shown in Equation 4.

$$d_{ij} = d(\tilde{x}_{jbD}, H_{abD} x_{iaD})^2 + d(x_{iaD}, H_{abD}^{-1} \tilde{x}_{jbD})^2 \tag{4}$$

In order to estimate correct matches m_{ab}, as shown in Figure 2.2, among all potential matches or correspondences, i.e. point pairs x_{ia} and $\tilde{x}_{jb}$ extracted from images a and b respectively, we used the overlap error as proposed in [**69**].

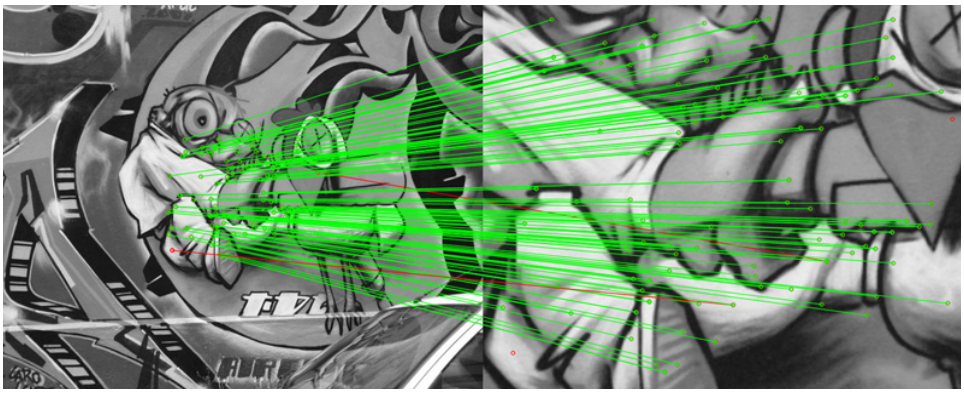

FIGURE 2.2. Correct matches(in green), wrong matches(in red) between two images.

This error measures how well two supporting regions, usually ellipses or circles R_{ia} and R_{jb}, estimated by point extraction algorithm from key points x_{ia} and $\tilde{x}_{jb}$ respectively, correspond under the known geometric transformation H_{ab}. In our case, this transformation is described by an homography.

$$\epsilon_s \leq 1 - \left(\frac{R_{ia} \cap H_{ab}^T R_{jb} H_{ab}}{R_{ia} \cup H_{ab}^T R_{jb} H_{ab}} \right) \tag{5}$$

The point pair x_{ia} and $\tilde{x}_{jb}$ that has lower error distance d_{ij} given by equation 4 and the lower overlap error given by equation 5 is considered as a true match. The overlap error reduces the probability of false positive matches. We calculate the ellipses overlap by using the software proposed in [**72**] and freely distributed by the author at `'www.chraibi.de'`.

4. Image Dataset

4.1. Acquisition Setup. Our image acquisition setup is composed by a DSLR Canon 7D and an iPad with a 5 Mega pixels built-in camera. In the Canon 7D scenario we used a Tamron 17-50mm f2.8 and a Canon 100mm f2.8 macro lenses. In addition to the camera, we used two Canon 580EXII flash with light diffuser, both operated wirelessly and synchronized with the acquisition. In the case of the iPad setup we can not synchronize the light with the acquisition, so we decided to use continuous light source instead of flashes.

4.2. Geometric transformations. In order to generate a set of images with perspective distortion, we carried out an approach similar to [**67**]. We used a Kuka robotic arm with a Canon 7D attached with Tamron lens in order to generate different points of view of the same target, as shown in Figure 2.3. The use of the robotic arm allowed us to generate known, repeatable and precise positions and trajectories around the target scene. We also used a Wacom Cintiq screen for displaying images instead of using pictures placed in a wall or in a table, as in [**67**]. Our set of displayed images covers different types of images with structured or unstructured textures, with low texture, or with repeating textures or patterns. Many authors [**59**, **63**, **67**] agreed in the importance of evaluating key point extractors and descriptors in such different conditions, in order to truly evaluate the robustness of their approaches.

The robotic arm is a KUKA LWR IV+, which has 7 joints, a payload of 7 kg and a repeatability of $\pm$ 0.05 mm. The desired position and orientation of the robot's end effector can be commanded from a remote PC, using the KUKA Fast Research Interface (FRI). The FRI provides a C++ high level interface, which can be used to retrieve information of the robotic arm, such as the tool's Cartesian position/orientation, and to implement different control strategies.

We decided to generate circular trajectories (arcs) to obtain several points of view of the Wacom screen, and therefore different values of captured perspective distortion. The desired circular path is defined by three points in the Cartesian 3D space, which are used to calculate the different elements of the parametric equation of a circle. The required orientation of the camera at the initial and final points of the trajectory can be defined independently of the circular path, allowing different configurations in a flexible fashion.

The described trajectories are resampled according to a desired number of points M along them, where images are to be taken. The set $Q = \{Q_1, Q_2, \dots Q_M\}$ constitutes the resulting discretized trajectory. Each $Q_i \in Q$ is 3x4 matrix that describes the i pose (position and orientation) of the camera, with respect to the robot's base coordinate system, where $1 \leq i \leq M$. This means that the original circular path is approximated in a piecewise linear way. Analogously, the orientation of the camera at each Q_i is determined by performing a linear interpolation of the total rotation matrix R_T, defined by $R_T = R_M(R_1)^{-1}$, where R_M and R_1 correspond to the rotation parts of Q_M and Q_1 respectively. Therefore, R_T is applied in $M - 1$ steps, which can be done easily using quaternion notation.

Each element of Q is used as a set point for the robot's Cartesian controller. The points in Q set are traversed in order. When the position and orientation errors with respect to a particular point Q_i are below some predefined thresholds, a signal is sent to the camera in order to take N pictures in a synchronous way. At any point Q_i the first picture to be taken corresponds to the calibration pattern image; then $N - 1$ pictures of other images shown on the Wacom Cintiq screen are taken. While pictures are being taken the robot holds its position.

Figure 2.5 shows a 3D reconstruction of a known generated arc trajectory of the camera around the Wacom screen, from a circular sector of radius equal to 0.4m, covering a total angle of 70 degrees.

We used the calibration pattern image for calibrating the camera, i.e. estimate extrinsic and intrinsic parameters, and also for accurate estimation of the homographies between images.

We used the estimated camera calibration parameters for rectifying the distortion of the images acquired with the Tamron lens, which has around a 2% of geometric barrel distortion. The Canon 100mm macro lens is able to render images with almost negligible geometric distortions. Geometric distortion can be considered as one of many types of optical aberrations. These distorsions cause to the projection of incoming rays to the optical system differ from the ideal position produced

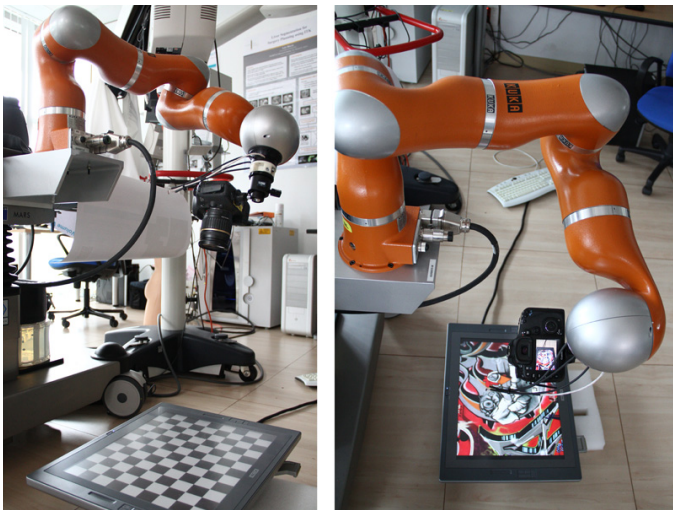

FIGURE 2.3. Image acquisition setup with Kuka robot arm and Canon 7D attached.

FIGURE 2.4. Some images of exposure varying dataset compound of 15 different images.

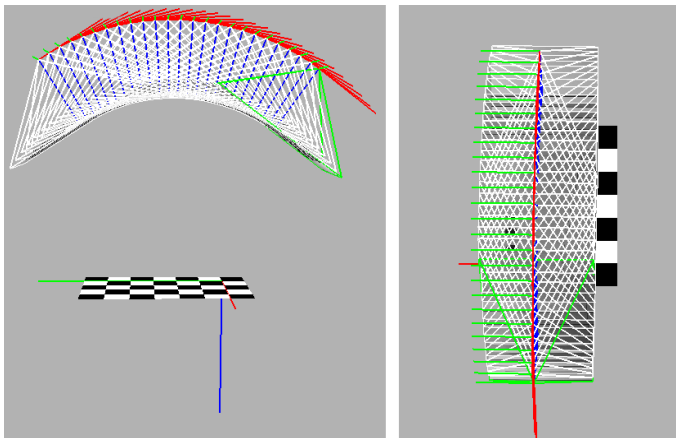

FIGURE 2.5. Recovered trajectory of a Robot driven image acquisition.

by a distortion free model, such as a pinhole camera. All images of our dataset are geometrically corrected, thus neither barrel nor pincushion distortions remain.

4.2.1. *Image Focus.* In addition to the capability of generating unfocused images with our image testing generator, we also captured real scenes because unfocused images are not only Gaussian smoothed versions of a correctly focused image. The shape of the lens diaphragm and the value of the lens aperture, which determines depth of field, play an important role in the finally rendered image; therefore it is not easy to simulate them synthetically. We propose an image dataset where the focus point is progressively varying from a correct focus point, i.e. all objects in the scene are accurately rendered in images as sharp, to a point where all objects appear blurred or unfocused, as shown in Figure 2.6.

FIGURE 2.6. Some images of focus varying dataset compound of 25 different images.

4.3. Photometric Transformation. Photometric transformations are also involved in the process of image formation along with geometric transformations. These transformations are related to the camera settings, light conditions and the nature of the camera hardware, mainly the camera sensor. As a photometric transformation dataset, we propose a set of images that show a variation in the light condition or light exposure, as shown in Figure 2.4. The purpose of this subset is to be able to evaluate the robustness of key point extractors repeatability or feature descriptors robustness against illumination changes and noise.

Image acquisition was carried out by using a protocol where no geometric transformations were applied between any of the images that form this dataset, ensuring that only photometric transformations occur between them. This implies that the homography matrix that relates them geometrically correspond to the identity matrix. To ensure that no geometric transformations were applied during dataset acquisition, both the illumination equipment and the camera were operated remotely. As mentioned in section 4, we used flashes to generate the illumination of the scene. The use of the flashes allow us to vary the amount of light without changing any camera acquisition parameters, i.e. setting fixed the aperture value, the exposure time, and ISO speed. In this way, neither the depth of field (DOF) is varied along the images that constitute the dataset, nor additional noise is added due to an increase of either ISO speed, or due to sensor heat because of longer exposure times. Every image in this dataset is consecutively reduced approximately an 1/3 of a f-stop, starting with a correct exposure in the first image. This dataset is composed of 15 images resulting in a difference of 4.5 f-stops between the first and last images.

Figure 2.7 shows two images of the same scene taken with the iPad in controlled illumination conditions. Left image was captured with a correct value of exposure, while the right image was captured with approximately 2'5 f-stops less of exposure. As mentioned in section 4, in the mobile device setup we used a continuous light source where light intensity can be set manually. It is worth mentioning that both the focus point and exposure metering point were fixed along the capturing of all images in the dataset.

In opposite to the DSLR setup where exposure values, i.e. ISO speed, aperture, and exposure time, can be set manually, in a mobile device, such as the iPad, those values are set automatically during image acquisition. In this way, we used an application that allowed us to focus and measure exposure always in the same gray neutral part of the scene along the captures. This ensures that the

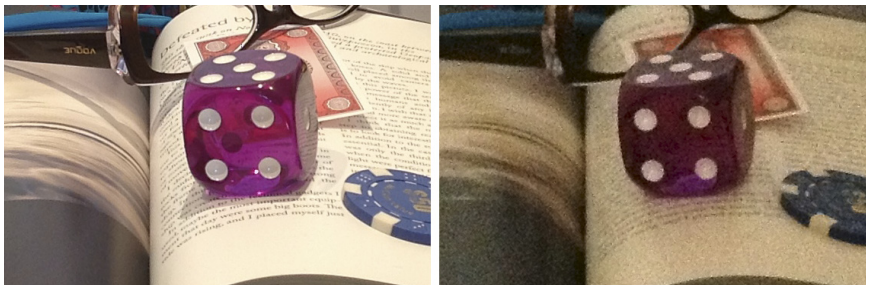

FIGURE 2.7. Images from the photometric Noise transformation taken with a mobile device.

exposure readings are consistent along image acquisitions, given different light conditions. As expected, in both cases, as the amount of light decreases, i.e. the signal-to-noise ratio (SNR) decreases, the amount of digital noise increases. This is clearly more noticeable in the case of the mobile device, due to the smaller size of its image sensor, and therefore a more limited dynamic range compared with the DSLR camera.

5. Synthetic Image Dataset Generator

In addition to the proposed set of images, we implemented a set of C++ functions and Python Scripts that allow the generation of several testing images by applying either random or systematic geometric transformations, as well as photometric transformations. Through Python scripts the user can define the source image, the type of transformation, the number of images to be generated, and the minimum and maximum values for the given transformation. In this way, it is easy to generate several datasets, with different types of images, and several types of transformations and transformation ranges. Next, we describe the type of transformations implemented in the image generator.

5.1. Geometric transformations. The proposed testing image generator allows to generate transformed views of a source image by applying similarity transformations such as isotropic scaling, or in-plane rotation, as shown in Figure 2.8, as well as other affine transformations in one or several directions. The generation of this type of images is useful in order to evaluate the behaviour of different approaches against different values of a given transformation, as described in section 3.

5.2. Photometric Transformation. In our transformed image generator, we also incorporated a functionality that allows to generate images contaminated with noise. Digital image noise can be split mainly in two different categories, luminance noise and chrominance noise, depending if the errors are produced in luma (intensity) or in chroma (color). There are some others types of noise such as horizontal or vertical banding (patterned noise), but it does not degrade images as luminance or chrominance noise do. Our image generator is able to create images contaminated with luminance or chrominance noise, or with both types simultaneously.

Figure 2.9 shows, from left to right, an image patch filled with 50% gray value, contaminated with luminance noise only, with chrominance noise only and with both types of noise simultaneously. Depending on the nature of the camera and acquisition, i.e. exposure and ISO speed, these errors may vary. For example, we can check in the images of light varying dataset how noise levels increase as light decreases (SNR decreases), which is more noticeable in the case of the iPad.

6. Conclusions

We have presented a new set of images, as well as an image generator and an evaluation framework that help in the evaluation and development of new approaches related with image key point extraction, description and matching for both standard and mobile devices. Our proposed framework can be seen as an extension or an evolution of the extensively used evaluation framework of [**69**].

FIGURE 2.8. Scale transformed views of the first image of the Graffiti dataset, proposed in [**69**]

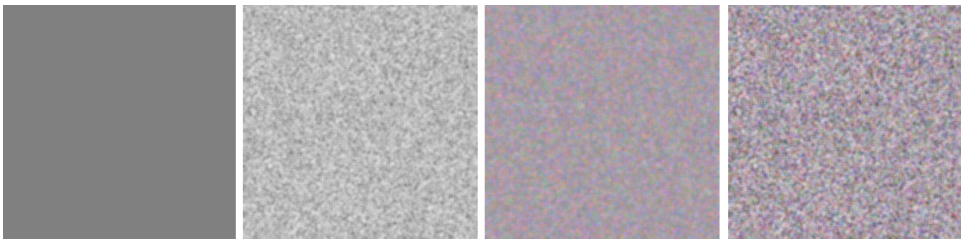

FIGURE 2.9. Types of noise

Moreover, the proposed image dataset has a higher number of images, with higher resolution and with better controlled geometric and photometric conditions. The evaluation framework is entirely written in C++, and therefore easily integrable in many research environments related with the testing or development of key point extraction, description and matching mechanisms.

We are currently using and extending our proposed framework for the evaluation of state-of-the-art approaches for key point feature descriptors, such as BRIEF, ORB, RIFF, sGLOH, FREAK, NERIFT, or BRISK, among others, with real acquired images, as well as with synthetically generated ones.

CHAPTER 3

Sensitivity Analysis of Optimized Curve Fitting to Uniform-noise Point Samples

CONTEXT: A project to reconstruct curves from noisy point samples was developed at the CAD CAM CAE Laboratory of the Universidad EAFIT. The mentioned application is needed for surface reconstruction in many fields, including the processing of medical images. In the medical field, the results of surface reconstruction are widely used in image guied surgery and diagnotic procedures. The implemented methodology performs the curve reconstruction using parametric curves. The results of this research provide an optimized curve fitting method and a sensitivity analysis of the parameters of the optimization problem.

This work has been founded by Universidad EAFIT and the Colombian Council of Research and Technology (COLCIENCIAS). Camilo Cortes, research assistant under my direction in the CAD CAM CAE Laboratory, was able to program the application of the devised methods. The contributions of this work have been published in:

Sensitivity Analysis of Optimized Curve Fitting to Uniform-noise Point Samples. Oscar E. Ruiz, Camilo Cortes, Diego A. Acosta and Mauricio Aristizabal. Proceedings of the 9th International Symposium on Tools and Methods of Competitive Engineering (TMCE 2012). ISBN 978-90-5155-082-5, pp 671-684. May 7-11, 2012. Karlsruhe, Germany.

Additionally, the authors have been invited to publish and extended version of this article for a special issue of the journal Computers in Industry, which is to be submitted in few months.

- Oscar E. Ruiz[1]
- Camilo Cortes[1]
- Diego Acosta[2]
- Mauricio Aristizabal[1]

[1] CAD CAM CAE laboratory, Universidad EAFIT
Carrera 49 No 7 Sur - 50, Medellín, Colombia
[2] Research Group DDP, Universidad EAFIT
Carrera 49 No 7 Sur - 50, Medellín, Colombia

As co-authors of such publication, we give our permission for this material to appear in this document. We are ready to provide any additional information on the subject, as needed.

Prof. Dr. Eng. Oscar E. Ruiz
oruiz@eafit.edu.co
Coordinator CAD CAM CAE Laboratory
EAFIT University, Medellin, COLOMBIA

ABSTRACT. Curve reconstruction from noisy point samples is needed for surface reconstruction in many applications (e.g. medical imaging, reverse engineering, etc.). Because of the sampling noise, curve reconstruction is conducted by minimizing the fitting error (f), for several degrees of continuity (usually C^0, C^1 and C^2). Previous works involving smooth curves lack the formal assessment of the effect on optimized curve reconstruction of several inputs such as number of control points (m), degree of the parametric curve (p), composition of the knot vector (U), and degree of the norm (k) to calculate the penalty function (f). In response to these voids, this article presents a sensitivity analysis of the effect of m and k on f. We found that the geometric goodness of the fitting (f) is much more sensitive to m than to k. Likewise, the topological faithfulness on the curve fit is strongly dependent on m. When an exaggerate number of control points is used, the resulting curve presents spurious loops, curls and peaks, not present in the input data. We introduce in this article the spectral (frequency) analysis of the derivative of the curve fit as a means to reject fitted curves with spurious curls and peaks. Large spikes in the derivative signal resemble Kronecker or Dirac Delta functions, which flatten the frequency content ad-infinitum. Ongoing work includes the assessment of the effect of curve degree p on f for non-Nyquist point samples.

Keywords: Parametric curve reconstruction, Noisy point cloud, Sensitivity analysis, Minimization.

Nomenclature

C_0	Unknown C^1-derivable simple planar curve
C(u)	Parametric planar curve approaching C_0
C(u_i)	Point on C(u) closest to cloud point p_i
d(p,S)	Distance from point p to the point set S
k	Degree of norm: $(\Sigma\|x_i\|^k)^{1/k}$
l	Length unit
m	Number of control points of $C(u)$
P	$[P_0, P_1, ..., P_{m-1}]$. Control polygon of $C(u)$
PCA	Principal Component Analysis
PL	Piecewise Linear
S	$\{p_0, p_1 ..., p_n\}$ Noisy point sample of C_0

1. Introduction

Many engineering applications need to recover a planar curve from a noisy point sample. A possible approach is to fit a curve to the point set, recognizing the stochastic nature of the data. This approach consists in adjusting a parametric or implicit curve to the set of points by minimizing an unsigned distance function between the points and their approximating curve. In the existing literature this approach is reported in the form of heuristic - based experiments. The heuristics used affect the number of control points of the curve, its degree, the norm used to measure distances, the knot vector for the parametric curve, etc. However, it must be noticed that a numerical systematic evaluation of the importance of these factors is not reported.

This article presents a discussion of the optimality conditions of the curve fitting problem with b-splines [**73**] of the type Open, Uniform, degree 2, whose knot vector was adjusted such that $0 \leq u \leq 1$. Our analysis and results apply for other curve types, although not with the same quantification. In this article we address point samples with uniform sampling noise, leaving spatial-dependent noise for future publications.

1.1. Curve self-intersection. Fig. 3.1 illustrates that, in the presence of sampling noise, it might be immaterial whether the sampled curve C_0 is self-intersecting or not. In the examples shown, the point sample will indicate a self intersecting curve in either case. We declare here that the issue of self-intersection of C_0 is outside the scope of this article and therefore we will consider open,

simple (i.e. non self - intersecting) curves. We introduce the issue only for establishing a context for the term *self - intersection*.

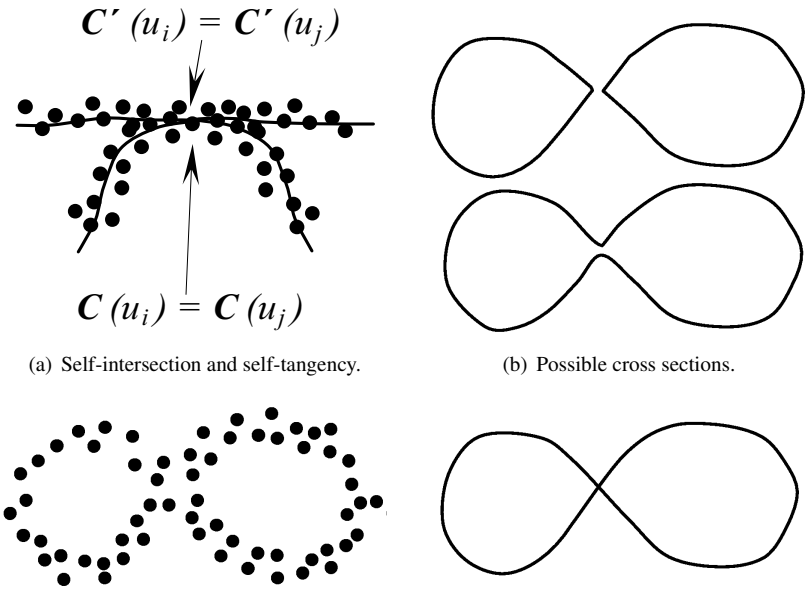

(a) Self-intersection and self-tangency.

(b) Possible cross sections.

(c) Point sample of the cross sections.

(d) PL approximation (non-manifold) of the cross sections.

FIGURE 3.1. Ambiguous noise sample of near self-intersecting curves. [**74**].

1.2. Objective function. In mathematical programming, an objective or cost function f is a function that represents how a dependent variable of a process (e.g. profit, cost, energy, etc.) behaves in terms of a set of independent or decision variables. Depending on the nature of the optimization problem the objective function is maximized or minimized by tuning the independent variables.

In the context of reverse engineering the problem of parametric curve reconstruction from noisy point samples can be stated as follows:

Given an unknown target curve to reconstruct C_0, whose sampling (possibly noisy) constitutes a point set S, find a parametric curve C, which approximates C_0 by minimizing the distance between the curve and the elements of S. In general, the following expression is used to measure the fitting error and therefore is the objective function to be minimized:

$$f = \sum_{i=1}^{n} d_i^w \tag{6}$$

where the residual d_i represents the minimum distance between the i-th cloud point and the curve C. w indicates the order of the residual. Then d_i is given by:

$$d_i = \min_{C(u)\in C} \|C(u) - S_i\|^k \tag{7}$$

where k is the norm-degree to calculate the distance.

Sections 2.1 and 2.2 discuss the objective functions used in curve fitting and the strategies to calculate the residuals d_i.

1.3. Decision variables and parameters of the optimization problem. As seen in 1.2 there are plenty of terms involved in the calculation of Eq.6 that can be tunned to minimize it.

An option is to fit variables inherent to the definition of the parametric curve C.

If C is a b-spline curve, then m, P, the curve degree p and knot vector U can be adjusted to improve the fitting to S. In the literature the most common approach is the optimization of P, sometimes supplemented with the adjustment of U as found in [**75**]. On the other hand, the terms involved in the calculation of the objective function f such as k and w can be set to produce the desired results.

In our approach the decision variables are the control points P. All other terms remain constant and are considered parameters of the problem (i.e. norm k, number of control points m, knot vector U and curve degree p).

1.4. Constrains and degrees of freedom. Most optimization problems include some constrains on the decision variables, which bound the region of search of an optimal solution. In the context of curve fitting to noisy data sets some constrained approaches have been developed. In section 2.1 a brief reference to them is performed. In our implementation there are no constrains on the decision variables. As is discussed in the following sections this fact is decisive in the determination of the uniqueness of the solution and its global scope. This optimization problem is classified as Non-linear unconstrained.

The degrees of freedom G of an optimization problem are given by the subtraction of the number of the number of equality constrains E from the number of decision variables V ($G = V - E$). Optimization techniques are used to solve underdetermined systems, which means $G > 0$. Notice that for curve fitting problems in which only the control points are adjusted, the number of decision variables is $2m$ when implementing planar curves and $3m$ for the case of curves in the euclidean three-dimensional space. As our development is performed using planar curves and there are no equality constrains $G = 2m$.

1.5. Sensitivity analysis. This analysis consists of studying how the objective function behaves when the parameters are perturbed. The calculation of the relative sensitivity allows to determine which parameter influences f the most .

Let $F(K, Q)$ be the objective function of an optimization problem where K is a decision variable and Q is a parameter. Then the relative sensitivity of $F(K, Q)$ with respect to Q, S_Q^F, as can be found in reference [**76**], is given by:

$$S_Q^F = \frac{\partial F/F}{\partial Q/Q} = \frac{\partial ln(F)}{\partial ln(Q)} \tag{8}$$

The value of S_Q^F is the ratio between the percent change in F and the percent change in Q, which is dimensionless. For this reason it is possible to compare the relative effect of each parameter on the objective function.

When the required derivatives are difficult to calculate the sensitivity must be calculated numerically as shown in [**77**, **78**]. In this paper the sensitivity analysis is performed to determine the influence of the number of control points m and the norm k on f.

1.6. Convexity. The objective function and search region convexity determine the classification and scope of an optimization problem solution. Let $\vec{x}$ be the decision variables vector of an optimization problem with objective function f. Let $\vec{x^*}$ be such that $\nabla f(\vec{x^*}) = 0$. Then, the assessment of the convexity of f at $\vec{x^*}$ allows to determine if $f(\vec{x^*})$ is a local extremum. If the optimization problem includes equality and inequality constrains, the convexity of the bounded region must be verified in order to conclude the uniqueness of the extremum, as discussed in [**76**].

In the case of the objective function, its convexity is evaluated using the eigenvalues of its Hessian matrix $H_f(\vec{x^*})$, which is defined in [**79**] as:

$$H_f(\vec{x}) = \left[\frac{\partial^2 f}{\partial x_i \partial x_j}\right]_{ij} \tag{9}$$

The eigenvalues e obtained from solving $det\left[H_f(\vec{x^*}) - eI\right] = 0$ indicate whether the function is convex, non-convex or a saddle point at $\vec{x^*}$. Furthermore, if $f(\vec{x^*})$ is optimized on a convex region, global maximum and minimum will be calculated as shown in [**76**].

2. Literature Review

Very few discussions about some important concepts inherent to mathematical optimization can be found in the curve fitting literature because most of the research is focused on exploring better algorithms to perform the optimization of the decision variables.

2.1. Objective function. As discussed in section 1.2, Eq.6 is the general representation of the objective function in curve fitting problems. Reference [**80**] employs first order residuals ($w = 1$) and references [**81–84**] use second order residuals ($w = 2$).

Some references add a smoothing term f_c to the objective function in order to adjust the final roughness of the curve:

$$f = \sum_{i=1}^{n} d_i^w + \lambda f_c. \tag{10}$$

The term f_c may contain information on the curve's first and second derivatives as in [**81**,**82**,**85**] or only information of the former as in [**80**, **86**] and λ determines its influence, penalizing large curvatures. Notice that penalizing the curvature prevents the curve fitting for non-Nyquist samples.

Some authors have explored constrained approaches. Reference [**86**] presents constrained curve and surface fitting to a set of noisy points in the presence of obstacles, which are regions that the curve or surface must avoid. Reference [**85**] considers the problem of curves that must lie on a 2-manifold (surface) also with forbidden regions. These procedures are implemented using a constrained non-linear optimization strategy.

2.2. Distance measurement. As seen in section 1.2 Eq.7 corresponds to the calculation of the distance d_i, which represents the residuals of the objective function in Eq. 6. In Curve Fitting algorithms the norm k is usually chosen to employ the Euclidean distance [**81**, **82**]($k = 2$).

The exact calculation of d_i is expensive, since it is obtained by a minimization procedure at each fitting iteration. The procedure consists of finding the parameter u_i which associates a point on the curve $C(u_i)$ with the i-th cloud point p_i such that d_i is a minimum, namely

$$\|C(u_i) - p_i\|^k = \min_{C(u)\in C} \|C(u) - p_i\|^k \tag{11}$$

The minimum distance is obtained performing an orthogonal projection of the point p_i to the curve C, which occurs when the dot product between the tangent vector at $C(u_i)$ and the distance vector d_i is null (see Eq. 12). Therefore, an alternative to face this problem is to solve for u in $g(u) = 0$ using the Newton's Method, as implemented in references [**73**, **82**]. Other approach is to minimize $g(u)$, references [**81**, **84**], for curve fitting, and [**80**], for surface fitting, propose the use of Newton-like iterative schemes, while [**87**] employs a gradient method. On the other hand, reference [**83**] implement a Genetic Algorithm to obtain the parameter u_i at each iteration of the minimization procedure.

$$g(u) = \left|C'(u) \cdot (C(u) - p_i)\right| \tag{12}$$

The approaches previously mentioned have drawbacks inherent to numerical methods, such as the need of a good initial guess, poor convergence and stagnation at local minima. These issues may lead to poor approximations of the distance d_i yielding unsatisfactory results of the fitting procedure.

Methodologies to automatically calculate an adequate initial guess for u in $g(u) = 0$ have been presented in literature. They are based on the point cloud subdivision using quadtree [**81**], k-D tree (for general dimensional fitting [**84**]) and Euclidean minimum spanning tree [**82**] strategies.

Different methodologies to measure the point-to-curve distance have been proposed, which are summarized as follows: (i) Point distance, which preserves the Euclidean distance between the cloud point and the paired point of the curve, discussed in [**81**, **85**], (ii) Tangent distance, which only preserves the distance between the cloud point and the tangential line projected at the paired point [**88**], and (iii) Squared distance, which is a curvature-based quadratic approximation of d_i^2 [**81**]. Reference [**84**] presents a deep comparison between these methodologies.

It must be also remarked that using the point-to-curve distance does not make the method sensitive to curls and loops (formed outside the S boundaries) and outliers in the final curve C. Because of these reasons, in our work we have included both the point-to-curve and curve-to-point distance calculation (in approximate manner), giving emphasis instead to curl and outlier avoidance.

2.3. Optimality conditions and sensitivity analysis. Regarding the number of control points m, reference [**75**] presents unconstrained and constrained approaches to solve the curve fitting problem to a set of low-noise organized data points using different values of m. The experiments performed show that increasing the number of control points helps, in general, to diminish f, although with the collateral effect of obtaining a more erratic curve.

Reference [**89**] shows similar results to [**75**] with the difference that the insertion and removal of control points is part of their fitting strategy. If the local approximation of a parametric curve segment is poor, a new control point is added to it. On the other hand, when redundant control points are detected in a curve segment, the control points of that segment are removed one by one taking care of not producing fitting errors above a defined threshold.

In this approach the curve to reconstruct is comprised by ordered dense data points. When working with highly noisy unordered data new challenges arise. In particular, the problem of finding and adequate number of control points for correct geometry and topology reconstruction has not been discussed throughly. For other parameters such as the norm k, the reported researches are oriented to identify which norm to use when certain features such as outliers and particular noise distributions are present in the point data set.

Reference [**90**] performs a comparison amongst L_1, L_2 and L_∞ norms in curve fitting applications with several data sets. In reference [**80**] curve and surface fitting case studies are presented using the L_1 and L_2 norm when the data set contains outliers. It is concluded that L_1 norm is less sensitive to outliers; therefore better results are obtained.

In summary, few discussions are presented about the influence of m and k on the behavior of f. Furthermore, a formal sensitivity analysis for these parameters has not been performed yet, to the best of our knowledge. In addition, some features of the optimization problem have not been discussed, such as the objective function convexity, and its role in extrema characterization.

2.4. Peaks, curls and closed loops detection. A mathematically optimal solution for the fitting curve problem does not necessarily imply a correct topological and geometrical reconstruction of the curve C_0 represented by the point cloud S. Some strong oscillations may appear during the fitting process, such as peaks, curls and closed loops. When pursuing the reconstruction of smooth simple curves (i.e. non-self-intersecting) these features are undesirable and may be avoided by finding an optimal value for m, as shown in this paper, as opposed to the strategy of curvature penalization implemented in [**80–82**, **86**].

The main drawback of the curvature penalization is that it is difficult to properly establish the weight λ with respect to the contributions of the distance residuals d_i in Eq.10, for each case study. Additionally, optimizing m results in an efficient use of the decision variables. Therefore, detection of peaks, curls and closed loops is necessary to find a reasonable number of control points.

In the literature, efficient methods to detect self-intersections can be found, covering the closed loops detection case. Reference [**91**] presents an algebraic approach to detect self-intersections solving $C(u) - C(v) = 0$, with u being different from v, and proposing a new function that does not contain zeros in this diagonal. In any case, peaks and curls detection is not a trivial and a method to detect all undesired features is necessary. In this paper we open the discussion of the use of the $C(u)$'s curvature information in the frequency domain to detect the presence of peaks, curls and closed loops.

2.5. Literature review conclusions and contribution of this article. According to the taxonomy conducted in this literature review, there are several issues that remain open in optimized curve fitting to point clouds. These subjects include: (a) Identification of the effect of the parameters such as the number of control points m, knot vector U and norm k in the curve fitting problem, (b) Detection of the presence of peaks, curls and closed loops in C to support the parameter optimal value identification and (c) Characterization of the curve fitting problem from the viewpoint of mathematical optimization.

In response to these issues, this article reports, in addition to formulating the optimization problem, the implementation of: (i) Sensitivity analysis of the number of control points m and norm k on f and (ii) Quantitative analysis of $C(u)$ curvature information in the frequency domain to detect the presence of peaks, curls and closed loops.

3. Methodology

3.1. Dual distance calculation. In addition to the point-to-curve distance introduced in section 2.2 the curve-to-point distance is used to calculate the distance d_i used in Eq.6, for the implementation of the curve fitting algorithm used in this research.

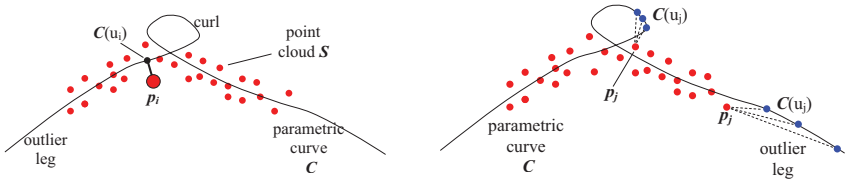

(a) Distances cloud point to curve. (b) Distances curve to cloud point.

FIGURE 3.2. Distances cloud points to/from curve.

When implementing the point-to-curve distance we define the residuals as

$$d_i = ||p_i - C(u_i)||^k \tag{13}$$

where u_i is the parameter in the domain of C which defines the point $C(u_i)$ closest to p_i. The term d_i represents the distance measured from each cloud point to the curve C (see Fig. 2(a)). This calculation of the distance between a point and an algebraic curve is a very expensive proposition because it implies the calculation of common roots of a polynomial ideal (see [**92**], [**93**]).

Notice that the vector $p_i - C(u_i)$ is normal to the curve C at the point $C(u_i)$. To avoid the computational expenses of algebraic root calculation, we approximate $C(u)$ in PL manner and calculate d_i simply by an iterative process. We sample the domain for $C(u)$, ($[0, 1]$) getting $u = [0, \Delta_u, 2\Delta_u, ..., 1.0]$ and approximate the current C curve with the poly-line $[C(0), C(\Delta_u), C(2\Delta_u), ..., C(1.0)]$. Calculating an approximation of $C(u_i)$ for a given p_i simply entails traversing $[C(0), C(\Delta_u), C(2\Delta_u), ..., C(1.0)]$ to find the $C(\kappa\Delta_u)$ closest to p_i.

Fig. 2(a) displays the distance from a particular (emphasized) cloud point p_i to its closest point $C(u_i)$ on the current curve C. Such a distance has influence in f as per Equation 6. Notice, however, that p_i and $C(u_i)$ (and hence f) do not change if large legs and curls appear in the synthesized C. Therefore, considering only the distance *from cloud points to the curve* in Eq.6 allows the incorrect formation of outlier legs and curls outside the boundaries of S.

If one can make spurious legs and curls to inflate the objective function f, the minimization of f avoids them. This is achieved by including the distances from *the curve points C_i to the cloud points p_i* (see Fig. 2(b)) to penalize in f.

For any point $p \in \mathbb{R}^n$, the distance of this point to S is a well defined mathematical function: $d(p, S) = \underset{p_j \in S}{min}(||p - p_j||^k)$. For the current discussion the points p are of the type $C(u_i)$ (i.e. they

are points of curve C). The u_i parameters to use are the sequence $u = [0, \Delta_u, 2\Delta_u, ..., 1.0]$, already mentioned.

Notice that $d(p, S) = ||p_j - p||^k$ for some cloud point $p_j \in S$. Let us define the point set A_j (on the curve C) as:

$$A_j = C(u)|u \in U \wedge d(C(u), S) = ||p_j - C(u)||^k \tag{14}$$

The set A_j contains those points in the sequence $[C(0), C(\Delta_u), C(2\Delta_u), ..., C(1.0)]$ that are closer to the point $p_j \in S$ than to any other point of S. We note with M_j the cardinality of A_j. Observe that some M_j might be zero, since p_j could be far away from be curve C and no point on the curve would have p_j as its closest in S. The set of all A_js could also be understood as a partition of the curve C.

With the previous discussion, a new definition of the residuals d_i, to be used in Eq. 6, is possible:

$$d_i = ||p_i - C(u_i)||^k + (\frac{1}{M_i}) \sum_{C_v \in A_i} ||C_v - p_i||^k \tag{15}$$

The $||p_i - C(u_i)||^k$ in Eq. 15 considers the distance from cloud points in S to the curve C. The term $(\frac{1}{M_i}) \sum_{C_v \in A_i} ||C_v - p_i||^k$ expresses distances from the curve C to the cloud points in S. This term penalizes the length of the curve, by increasing f.

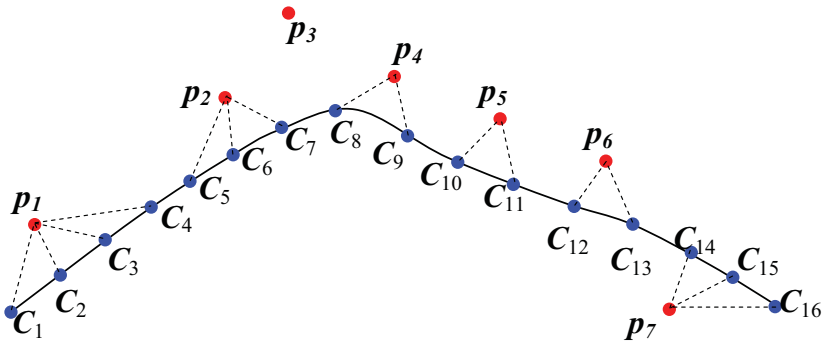

FIGURE 3.3. Clusters of distances from curve to cloud points.

Fig. 3.3 presents a rather simplified materialization of the situation, with very few cloud points, moreover biased with respect to the instantaneous C curve. However, it serves the purpose of illustrating the algorithm.

3.2. Convexity. Since the optimization problem that is attacked in this article has no constrains, only the convexity of the objective function is analyzed. The variables to minimize f are the x and y coordinates of the control points ($P_j = (x_j, y_j)$) contained in the control polygon $P = [P_0, P_1, ..., P_{m-1}]$; therefore, the corresponding Hessian matrix is given by:

$$H_f(P) = \left[\frac{\partial^2 f}{\partial P_i \partial P_j}\right]_{ij} \tag{16}$$

with

$$\frac{\partial^2 f}{\partial P_i \partial P_j} = \begin{bmatrix} \frac{\partial^2 f}{\partial x_i \partial x_j} & \frac{\partial^2 f}{\partial x_i \partial y_j} \\ \frac{\partial^2 f}{\partial y_i \partial x_j} & \frac{\partial^2 f}{\partial y_i \partial y_j} \end{bmatrix} \tag{17}$$

Numerical differentiation is implemented for the calculation of $H_f(P)$, using approximations for the second order and mixed derivatives. Next the eigenvalues of $H_f(P)$ are computed and the convexity or concavity of f is evaluated as discussed in 1.6.

3.3. Sensitivity calculation. In order to calculate the relative sensitivity of the objective function with respect to the parameters on a defined domain of each one of them, the curve fitting problem is solved for a set of parameter values. For a given value of the parameter, m_i or k_i (when computing S_m^f or S_k^f respectively), the curve fitting problem is solved obtaining a value of the objective function f_i. Notice that i indicates the number of increments applied over an initial value of the parameter of interest and goes from 0 to a defined number of maximum increments Max_{inc}.

Next, the sensitivity at an increment i ($0 \leq i < Max_{inc} - 1$) is numerically calculated by using the values of the parameter and objective function at i and $i + 1$ as discussed in 1.5. While calculating S_m^f, k is kept constant. Similarly, when computing S_k^f, m is kept constant.

The steps of this procedure are summarized as follows:

(1) *initialization*: The point cloud S, to be fitted is loaded. Depending on the sensitivity to be computed m_0 or k_0 is assigned with an initial value.
(2) *initial guess calculation*: A straight line L is used as an initial guess for the b-spline curve C. This allow us to provide an initial guess whose topology and shape is not affected by the number of control points used to build it. L is obtained performing a principal component analysis (PCA) (see reference [**74**]) over the whole S set. In the case of computing S_m^f the m_i control points are placed, equally-spaced, along L. When calculating S_k^f, the number of control points is kept constant, so that the initial guess will be the same during the whole procedure.
(3) *curve fitting*: A penalized Gauss-Newton algorithm is used to perform the adjustment of P. Once the stopping criteria is met, the value of f is saved as f_i.
(4) *parameter value increment*: The parameter value increment is defined as: m_{i+1}=m_i+1, for the number of control points and $k_{i+1} = k_i + \Delta k$, for the norm. Where Δk is an arbitrary small constant value. Only when $i < Max_{inc}$ the increment is performed and the process goes back to step 2, otherwise the procedure finishes.

In this article we analyze the sensitivity only with simple curves, ignoring for the time being self-intersecting curves.

3.4. Peaks, curls and closed loops detection approach. When solving the curve fitting problem some undesired features such as closed loops, curls and peaks may appear in the adjusting curve for certain configurations of parameters. The length and curvature of C can provide some information about the topology and geometry of the curve. However, without knowing what are the expected values for this metrics it is difficult to conclude from them the correct topological reconstruction of S, and therefore to establish an optimum value of the parameters of the problem. These reference values may be expensive to obtain in the preprocessing stage from the cloud point.

Adding information about the first and/or second derivatives of the curve to f helps to obtain smooth fitting curves. However, weighting factors between the contributions of the distance residuals (7) and curve derivatives to f must be defined, interactively, for every case of study (see references [**82**] and [**86**]) as a consequence of not having benchmark values for these measurements. Therefore it is desirable to devise a method to determine the presence of curls and peaks in the fitting curve without the high overheads derived form extracting reference values form the point cloud.

In this paper we propose to perform an analysis of the frequency spectrum of certain information of the fitting curve that reflects the presence of the undesired features previously mentioned. The representation of the data in the frequency domain indicates how it is composed of low and high frequency waves, making easier to establish whether the curve follows the desired behavior or not. This task is accomplished by studying the changes of direction of the first derivative of the curve with respect to its parameter u. Peaks and curls produce large sudden changes in the direction of $\frac{\partial \vec{C}}{\partial u}$ that are represented in the frequency domain with a considerable presence of high frequency sinusoidal curves.

We have obtained the frequency spectrum computing the discrete Fourier transform (DFT) of the previously mentioned data. To guarantee that the desired information is sampled according to the Nyquist criterion, for this process, is of prime importance. To achieve this, we have chosen a series of u parameters that are located at equal distances d_s, of each other, on the curve, constituting $u_s = \{u_0, \ldots, u_g\}$. We have chosen $d_s = 0.0001l$, where l is the unit of distance, thus the sampling frequency is $f_s = 10000l^{-1}$.

Next, the normalized tangent vectors of the curve were computed at all the points given by the parameters u_s obtaining $V_s = \left\{\hat{V}_0, \ldots, \hat{V}_g\right\}$. The dot product of every $\hat{V}_i$ and $\hat{V}_{i+1}$ pair is computed, where $0 \leq i \leq g-1$, and therefore the angle θ_i between them is obtained. Finally the magnitude of the DFT is obtained, and properly scaled to achieve a single-sided spectrum of power vs. frequencies of the obtained history of θ.

4. Results and Discussion

4.0.1. *Test point set.* The point cloud shown in Fig.3.4 was used to run the procedures discussed here and in the following sections. As in the sensitivity experiments, the fitting curve initial guess used here was a straight line obtained from a PCA of the complete point cloud. The Hessian matrix $H_f(P)$ and its eigenvalues e were calculated in every iteration of the optimization procedure using 5, 8, 9 and 15 control points.

4.1. Convexity. As discussed before, the region of search and objective function convexity is a necessary condition to claim the global scope of a solution of a minimization problem. Since the problem we deal with is unconstrained, the region of search is unbounded and its convexity can not even be verified. Therefore, by definition, the solutions found from the minimization procedure can only be classified as local. However the behavior of f is still of interest, since it hints to possible better results to be obtained .

For all these cases of study (5, 8, 9 and 15 control points) the convexity of f depends on the location of the control points P used to calculate $H_f(P)$, given that the eigenvalues obtained did not comply with the condition $e_j \geq 0 \ \forall j$, where $1 \leq j \leq 2m$, at certain iterations of such tests. Therefore, no unique extremum exists and only convergence to a local minimum can be guaranteed.

Because of the behavior of f, it is of prime importance to provide an initial guess for C close to a satisfactory solution avoiding large optimization times and stagnation in local minimum with poor topological and geometrical reconstruction.

4.2. Number of control points sensitivity calculation. The process was run twice with a number of control points ranging between 4 and 16, using both norms, L_1 and L_2. The results of S_m^f are summarized in Fig.5(b), where can be noticed that as m increased f became less sensitive to it, specially when using L_2 norm.

In addition to the value of f and S_m^f, the curve length and curvature were calculated to obtain information about the topology of the fitting curve (i.e. curls, peaks, long legs, etc). In this paper what is presented as curvature corresponds to the sum of the curvature at a determined number of samples along the curve.

The results show a general trend in which as the number of control points increases the objective function decreases (see Fig.5(a)). However, with exaggerated number of control points, given the topological situation, some undesirable features begin to appear, such as curve roughness, curls and/or peaks and attraction among control points. These outcomes were obtained with both of the norms tested (i.e. $k = 1$ and $k = 2$). In Fig.3.6 the resulting curves of the fitting with different number of control points are shown using L_1 and L_2 norms.

For the particular point cloud used in these tests the minimum number of control points to reconstruct its topology is 5. Increasing the number of control points does not yield in a considerable diminution of f and more importantly, a better topological reconstruction of the curve is not necessarily obtained.

With the usage of the dual distance in f (see 1.2), the peaks and curls that appear are located inside the boundaries of the point cloud S, and what they produce is a reduction of f. The excessive

amount of degrees of freedom of the curve allows the appearance of these curls and peaks, as the optimization algorithm place the control points minimizing the objective function.

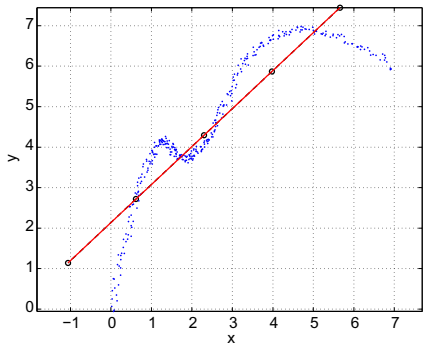

FIGURE 3.4. Point cloud and initial curve guess with five control points.

4.3. Norm sensitivity calculation. The relative sensitivity S_k^f was calculated from norm $k = 1$ to $k = 2$ with $\Delta k = 0.01$. The test was run twice, initially, with 5 control points, which are the minimum number of control points to successfully fit S, as determined in section 4.2, and then with 8 control points. The results show that small changes in the norm k may produce large relative changes in the values of f obtained in the domain defined by $1 \leq k \leq 2$ for both of the m tested. Figures 7(a) and 7(b) show an irregular behavior from which no particular value or range of k derive a remarkable improvement of the fitting.

It must be considered that even if the same curve topology and geometry are obtained implementing two different norms, the value of f will be distinct for each case, due to the modification in the residuals calculation in Equation 7. This fact magnifies the effect that k has on f and is the reason of the variability observed. However with respect to the quality (i.e. topology and geometry) of the curves obtained along the procedure (see Fig.3.8), the influence of k is almost imperceptible, when m is chosen properly.

The curve length and curvature in figures 7(c) and 7(d) reflect a very stable behavior as k changes using 5 control points. The outlier curve segments observed in Fig.3.8 when $m = 5$ can be adjusted changing the stopping criteria of the optimization algorithm, so a few more iterations are performed. On the other hand, using 8 control points some peaks and curls appear at certain values of k. This can be identified in a large increment in the curve length and curvature with respect to the values obtained for other norms implemented. Therefore, it is concluded that it is more effective to optimize m than k, in the pursuit of high topology and geometry fidelity in the reconstruction of S.

4.4. Peaks, curls and closed loops detection approach. The cloud point S to reconstruct and the procedure to obtain the fitting curve initial guess is the same implemented in previous sections. The methodology described in section 3.4 was applied for the fitting curves that resulted from the optimization procedure, using 5, 8, 9 and 15 control points, using only L_2 norm. The change of direction of $\frac{\partial \vec{C}}{\partial u}$, represented by θ, in degrees, is consigned in Fig.9(a) for all the cases of study.

In this figure it is shown how for the curves generated with 5 and 8 control points the magnitude of θ was kept small as C is traversed. When 9 and 15 control points were used, very large peaks were obtained in θ, in agreement with the presence of strong oscillations in the fitting curves.

In the frequency spectrum representation (see figure 9(b)), the θ data obtained when using 5 and 8 control points consist of very low frequency waves (i.e. near zero), while for the 9 and 15 control points cases the large peaks are represented by a considerable and stable presence of high frequency sinusoidal waves that go up to $5000l^{-1}$. Notice that this is the maximum frequency that can be

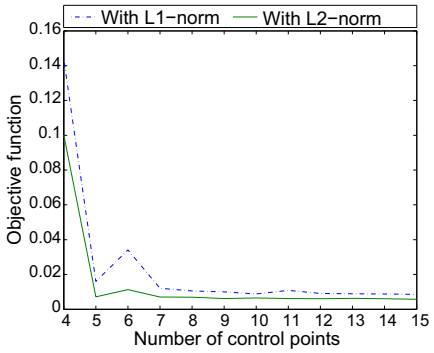

(a) Objective function vs. number of control points.

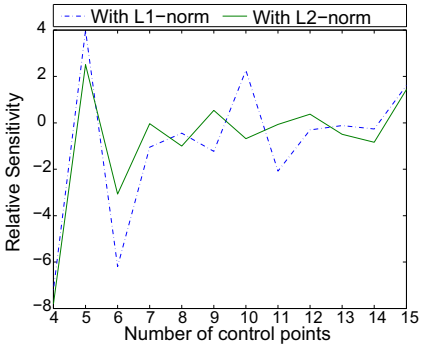

(b) S_m^f vs. number of control points.

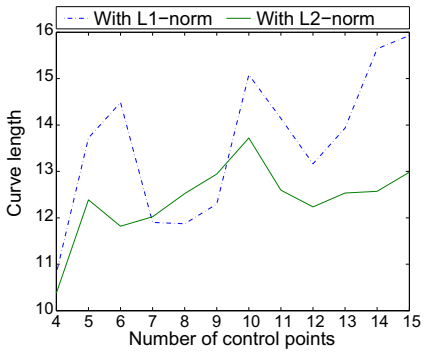

(c) Curve length vs. number of control points.

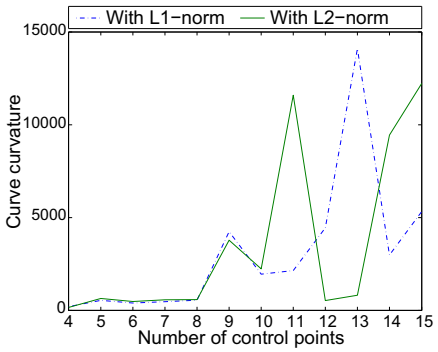

(d) Curve curvature vs. number of control points.

FIGURE 3.5. Resulting metrics of the fitting curve with different number of control points using L_1 and L_2 norms. Here the units of the length are l and the units of the curvature are $1/l$.

resolved according to the sampling rate implemented, but it is not the higher frequency of the waves that comprise θ for the later cases.

The information obtained from the frequency spectrum can be used to conclude the presence of peaks or curls in the fitting curve by comparing the contributions of low and high frequencies waves to θ. With the usage of the dual distance penalization, the curls an peaks in the fitting curve produce large values in θ because of their sharp shape, due to the fact that they are formed within the S boundaries. Therefore the low and high frequencies waves contributions to θ are very similar.

When optimizing the number of control points, the peaks and curls detection is useful to determine its upper limit, so the curve is not provided with an excessive degrees of freedom. If the optimization technique includes information about the curvature in f, the information obtained from the frequency spectrum can be processed to establish the weight of the curvature penalization in f dynamically.

5. Conclusions and future work

This article presented a sensitivity analysis of the number of control points m and norm k on the objective function f. It has been found that using an adequate number of control points the formation of peaks, curls and closed loops in C is prevented, making unnecessary to add a curvature penalization term to f in order to avoid them. Finding proper values of m also reduces the number

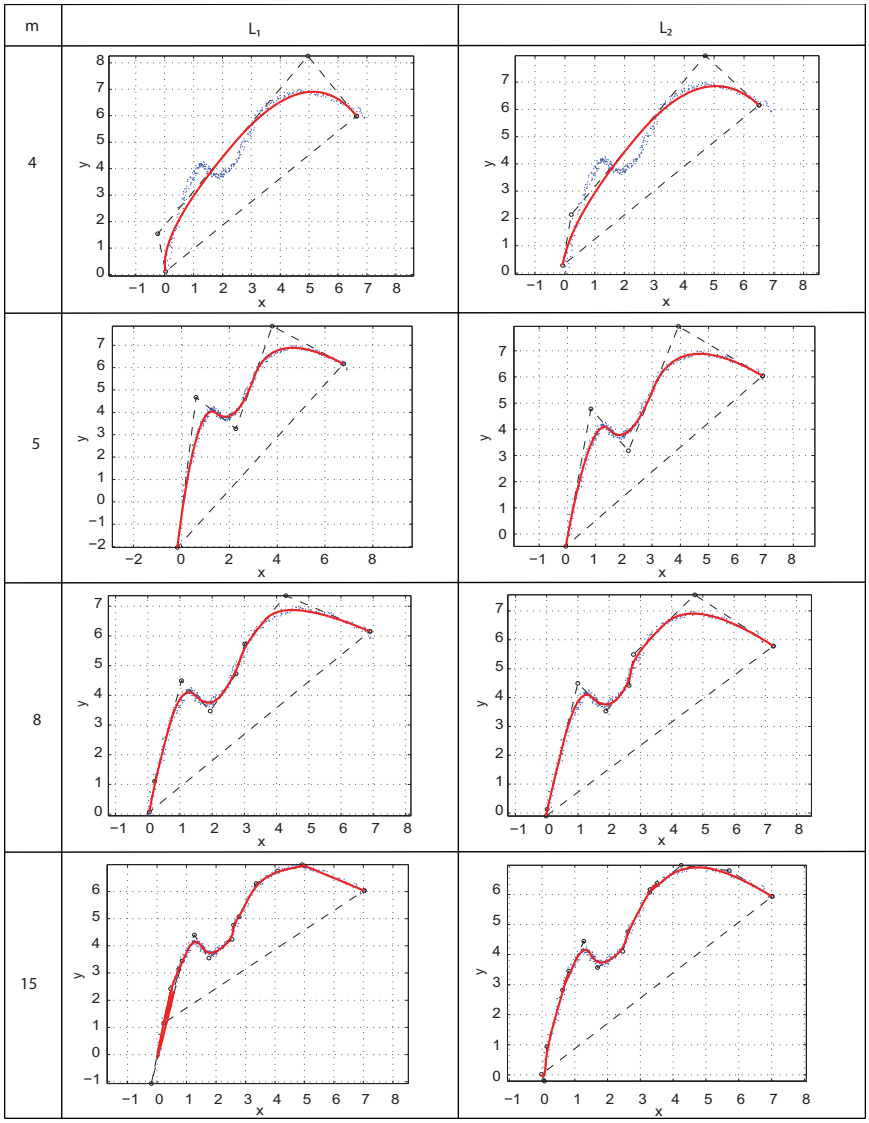

FIGURE 3.6. Resulting curves of the fitting with different number of control points m, using L_1 and L_2 norms.

of decision variables of the problem, which results in a more efficient process since redundancy of control points is avoided.

Changes in the values of k do not influence significantly the result of the reconstruction process when m is chosen properly. Although k produces larger percent changes in f than m, the optimization of m produce better results in terms of topology and geometry of the reconstructed curve. The analysis of the C curvature information in the frequency domain allows to identify the presence of peaks, curls and closed loops as they map into high frequency components in the frequency spectrum.

Ongoing studies are being undertaken to determine the influence of knot vector U and curve degree p on the minimization of the penalty function f, in case studies that include non-Nyquist and self-intersecting point samples. A remaining open issue is the implementation of a method that uses

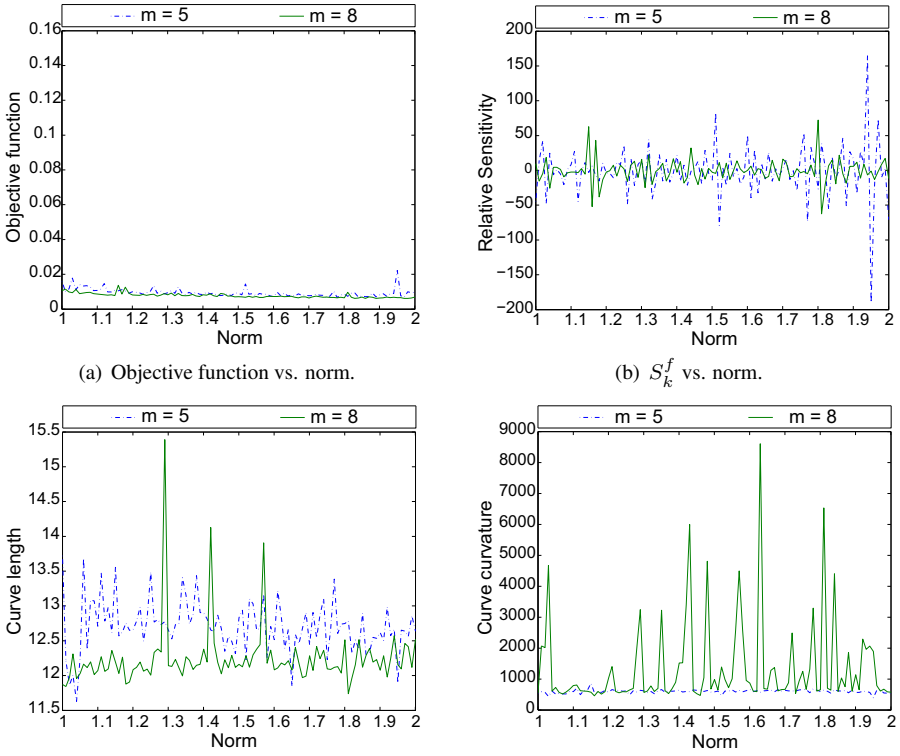

(a) Objective function vs. norm.

(b) S_k^f vs. norm.

(c) Curve length vs. norm.

(d) Curve curvature vs. norm.

FIGURE 3.7. Resulting metrics of the fitting curve with different norms using 5 and 8 control points. Here the units of the length are l and the units of the curvature are $1/l$.

information provided by the DFT of the curvature of C to find appropriate values for parameters such as m.

Notice that the complexity of the fast Fourier transform (FFT) and related efforts depends on the number of PL segments of the curve $C(u)$ (n: length of the θ history). It does not depend on the number of cloud points. The frequency content of the θ signal is obtained by using the FFT, whose complexity is $O(n.log(n))$. Although FFT has very reasonable computational expenses, more work is required in lowering the expenses of automatically analyzing the results of the FFT to detect curls and cusps.

Stochastic noise vs. Sampling Density. For a proper curve reconstruction the quality of the digitalization is of prime importance. If the sampling density and/or stochastic noise violate the Nyquist criteria, an accurate reconstruction becomes impossible. Further elaboration of this topic is left for future publications.

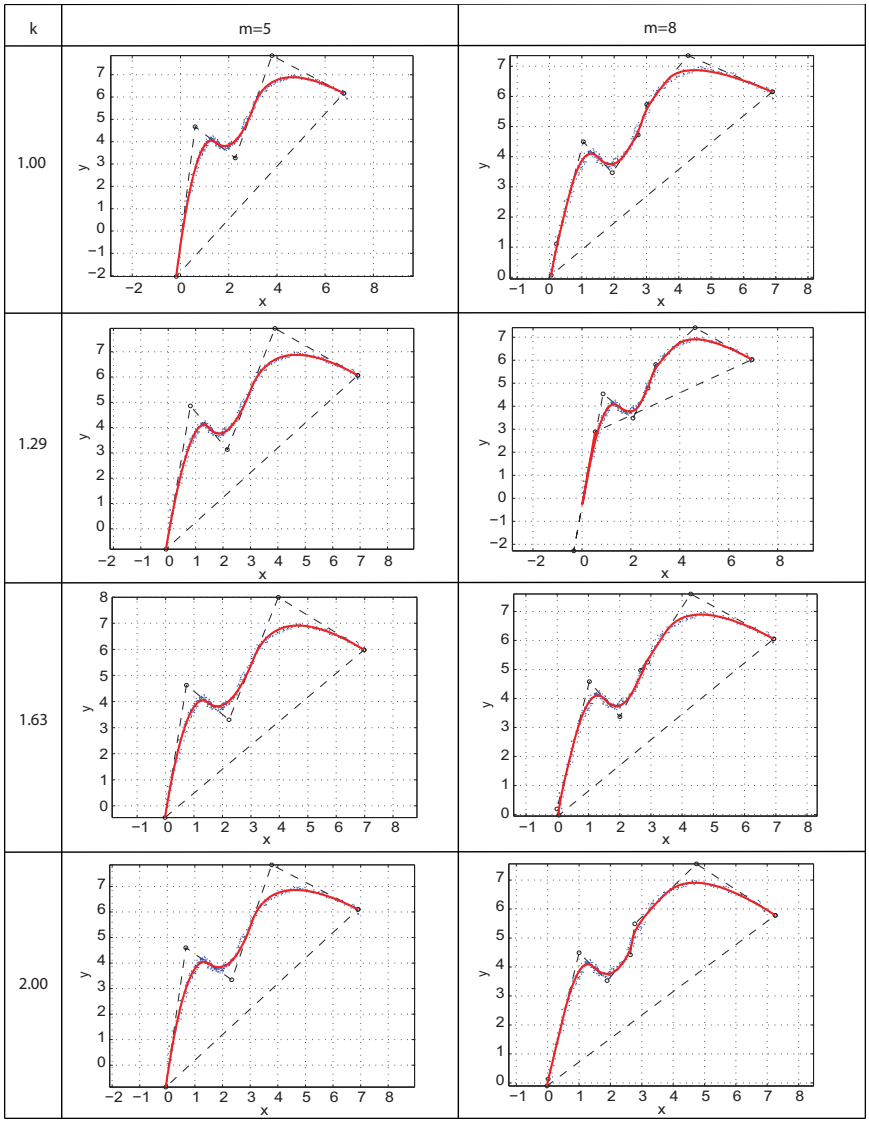

FIGURE 3.8. Resulting curves of the fitting with different norms k, using 5 and 8 control points.

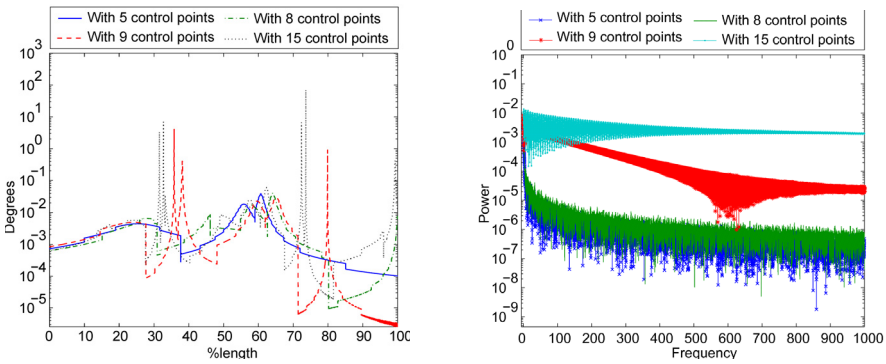

(a) Changes in direction of curve's first derivative (degrees) vs. length (percentage).

(b) Power vs. frequency.

FIGURE 3.9. Changes in direction of curve´s first derivative and frequency spectrum.

Conclusions

This works presents contributions to different procedures that are performed during the multiple stages that compose the medical workflow of common interventional procedures, such as preoperative and intraoperative ones. Through contributions to the solution of different problems in the field of medical robotics, computer vision and geometric modeling, applications such as medical imaging, patient registration, automatic endoscope positioning, augmented reality, robotic surgery, among others, can benefit from the presented developments.

To solve the challenges involved in the mentioned projects, different branches of knowledge were studied; these include: Computer graphics, Geometric Modeling, Optimization, Industrial and Medical Robotics, Haptics, Augmented Reality and Computer Vision. The interdisciplinary nature of such projects, conducted at CAD CAM CAE laboratory and Vicomtech, provided a very rich research experience. Also, this required high flexibility and adaptability in order to master the specific theory and technical skills needed to develop the required algorithms or to analyze the literature of such different fields. Here, it is interesting to note how the concepts of computational geometry are transversal to the mentioned areas, providing solutions from numeric, combinational and stochastic geometry. In this direction, the foundings I gained in the different subfields of computational geometry, during the first year of my master's studies, were fundamental to undertake the challenges involved in image guided surgery and medical robotics.

During the performance of the different research projects, it was of particular importance the interaction with physicians and surgeons as well as other people involved in the medical field, in order to capture their necessities and translate them into technological developments that they actually find useful and easy to integrate into their workflow. In this way, it is possible to define the requirements of each one of the layers of a product, such as a device or software, properly. Also, as a result of the mentioned interaction, the trends and future directions of the field are known at first hand. One of them, which I plan to address as future work, is the need for systems that help the surgeons to obtain information about the location of the anatomical structures to be dissected or preserved during surgery in real-time. This necessity is mainly induced by the complexity of certain interventional procedures, such as minimally invasive surgery, in which the sensory feedback of the surgeon is dramatically constrained. The required intraoperative assistive systems involve the development of flexible robotic platforms able to perform autonomous task or be telecommanded, real-time processing of medical images, such as ultrasound images, high precision tracking systems, and real-time patient registration methods.

Finally, as a conclusion of the whole reseach experience, I found invaluable the opportunity to know and interact with researchers, advisors and professors, of remarkable human and professional quality, at EAFIT and Vicomtech. The lessons that I have learned from them, have allowed me to improve skills in the research and human fields. Also, the experience of working and studying abroad has been of significant importance for my academic as well as for my personal formation.

Bibliography

[1] D.B. Camarillo, T.M. Krummel, J.K. Salisbury, et al. Robotic technology in surgery: past, present, and future. *The American Journal of Surgery*, 188:2–15, 2004.

[2] T. Haidegger and Z. Benyó. Industrial robotic solutions for interventional medicine. In *in Proc. of the Intl. GTE Conference MANUFACTURING*, pages 125Ű–130, 2008.

[3] H.I. Son, T. Bhattacharjee, and D.Y. Lee. Estimation of environmental force for the haptic interface of robotic surgery. *The International Journal of Medical Robotics and Computer Assisted Surgery*, 6(2):221–230, 2010.

[4] A. Simorov, R.S. Otte, C.M. Kopietz, and D. Oleynikov. Review of surgical robotics user interface: what is the best way to control robotic surgery? *Surgical Endoscopy*, pages 1–9, 2012.

[5] G.S. Weinstein, B.W. O'Malley Jr, S.C. Desai, and H. Quon. Transoral robotic surgery: does the ends justify the means? *Current opinion in otolaryngology & head and neck surgery*, 17(2):126, 2009.

[6] H. Mayer, I. Nagy, A. Knoll, E.U. Braun, R. Bauernschmitt, and R. Lange. Haptic feedback in a telepresence system for endoscopic heart surgery. *Presence: Teleoperators and Virtual Environments*, 16(5):459–470, 2007.

[7] T. Yamamoto, N. Abolhassani, S. Jung, A.M. Okamura, and T.N. Judkins. Augmented reality and haptic interfaces for robot-assisted surgery. *The International Journal of Medical Robotics and Computer Assisted Surgery*, 2011.

[8] A.M. Okamura. Haptic feedback in robot-assisted minimally invasive surgery. *Current Opinion in Urology*, 18:1–6, 2008.

[9] M. Tavakoli, RV Patel, and M. Moallem. A haptic interface for computer-integrated endoscopic surgery and training. *Virtual Reality*, 9(2):160–176, 2006.

[10] EP Westebring-Van Der Putten, RHM Goossens, JJ Jakimowicz, and J. Dankelman. Haptics in minimally invasive surgery-a review. *Minimally Invasive Therapy & Allied Technologies*, 17(1):3–16, 2008.

[11] O.A.J. van der Meijden and MP Schijven. The value of haptic feedback in conventional and robot-assisted minimal invasive surgery and virtual reality training: a current review. *Surgical endoscopy*, 23(6):1180–1190, 2009.

[12] A.M. Okamura. Methods for haptic feedback in teleoperated robot-assisted surgery. *Industrial Robot: An International Journal*, 31(6):499–508, 2004.

[13] C. Preusche and G. Hirzinger. Haptics in telerobotics. *The Visual Computer*, 23(4):273–284, 2007.

[14] M. Tavakoli, A. Aziminejad, R.V. Patel, and M. Moallem. High-fidelity bilateral teleoperation systems and the effect of multimodal haptics. *Systems, Man, and Cybernetics, Part B: Cybernetics, IEEE Transactions on*, 37(6):1512–1528, 2007.

[15] K. Ohnishi. Real world haptics and telehaptics for medical applications. In *Industrial Electronics (ISIE), 2010 IEEE International Symposium on*, pages 11–14. IEEE, 2010.

[16] K. Salisbury, F. Conti, and F. Barbagli. Haptic rendering: introductory concepts. *Computer Graphics and Applications, IEEE*, 24(2):24–32, 2004.

[17] J. Abbott, P. Marayong, and A. Okamura. Haptic virtual fixtures for robot-assisted manipulation. *Robotics Research*, pages 49–64, 2007.

[18] J.W. Park, J. Choi, Y. Park, and K. Sun. Haptic virtual fixture for robotic cardiac catheter navigation. *Artificial Organs*, 2011.

[19] SD Laycock and AM Day. A survey of haptic rendering techniques. In *Computer Graphics Forum*, volume 26, pages 50–65. Wiley Online Library, 2007.

[20] O. Weede, H. Monnich, B. Muller, and H. Worn. An intelligent and autonomous endoscopic guidance system for minimally invasive surgery. In *Robotics and Automation (ICRA), 2011 IEEE International Conference on*, pages 5762–5768. IEEE, 2011.

[21] U. Hagn, R. Konietschke, A. Tobergte, M. Nickl, S. Jörg, B. Kübler, G. Passig, M. Gröger, F. Fröhlich, U. Seibold, et al. Dlr mirosurge: a versatile system for research in endoscopic telesurgery. *International journal of computer assisted radiology and surgery*, 5(2):183–193, 2010.

[22] R. Kokes, K. Lister, R. Gullapalli, B. Zhang, A. MacMillan, H. Richard, and J.P. Desai. Towards a teleoperated needle driver robot with haptic feedback for rfa of breast tumors under continuous mri. *Medical image analysis*, 13(3):445–455, 2009.

[23] EU Schirmbeck, C. Haßelbeck, H. Mayer, I. Nágy, A. Knoll, FKB Freyberger, M. Popp, SM Wildhirt, R. Lange, and R. Bauernschmitt. Evaluation of haptic in robotic heart surgery. In *International Congress Series*, volume 1281, pages 730–734. Elsevier, 2005.

[24] Y.H. Kim, L.D. Phong, W.M. Park, K. Kim, and K.H. Rha. Laboratory-level telesurgery with industrial robots and haptic devices communicating via the internet. *International Journal of Precision Engineering and Manufacturing*, 10(2):25–29, 2009.

[25] H. Su, W. Shang, G.A. Cole, K. Harrington, and G.S. Fischer. Haptic system design for mri-guided needle based prostate brachytherapy. In *Haptics Symposium, 2010 IEEE*, pages 483–488. IEEE, 2010.

[26] H. Maass, HK Cakmak, UG Kuehnapfel, C. Trantakis, and G. Strauss. Providing more possibilities for haptic devices in surgery simulation. In *International Congress Series*, volume 1281, pages 725–729. Elsevier, 2005.

[27] SJ Phee, SC Low, ZL Sun, KY Ho, WM Huang, and ZM Thant. Robotic system for no-scar gastrointestinal surgery. *The International Journal of Medical Robotics and Computer Assisted Surgery*, 4(1):15–22, 2008.

[28] Z. Sun, Z. Wang, and S.J. Phee. Towards haptics enabled surgical robotic system for notes. In *Robotics, Automation and Mechatronics (RAM), 2011 IEEE Conference on*, pages 229–233. IEEE, 2011.

[29] T. Haidegger, B. Benyó, L. Kovács, and Z. Benyó. Force sensing and force control for surgical robots. In *7th IFAC Symposium on Modeling and Control in Biomedical Systems*, volume 7, 2009.

[30] P. Puangmali, K. Althoefer, L.D. Seneviratne, D. Murphy, and P. Dasgupta. State-of-the-art in force and tactile sensing for minimally invasive surgery. *Sensors Journal, IEEE*, 8(4):371–381, 2008.

[31] H. Tanaka, K. Ohnishi, H. Nishi, T. Kawai, Y. Morikawa, S. Ozawa, and T. Furukawa. Haptic endoscopic surgery robot utilizing fpga. In *Advanced Motion Control, 2008. AMC'08. 10th IEEE International Workshop on*, pages 601–606. IEEE, 2008.

[32] M. Mahvash, J. Gwilliam, R. Agarwal, B. Vagvolgyi, L.M. Su, D.D. Yuh, and A.M. Okamura. Force-feedback surgical teleoperator: Controller design and palpation experiments. In *Haptic interfaces for virtual environment and teleoperator systems, 2008. haptics 2008. symposium on*, pages 465–471. IEEE, 2008.

[33] S. Katsura, W. Iida, and K. Ohnishi. Medical mechatronics–an application to haptic forceps. *Annual Reviews in Control*, 29(2):237–245, 2005.

[34] T. Bhattacharjee, H.I. Son, and D.Y. Lee. Haptic control with environment force estimation for telesurgery. In *Engineering in Medicine and Biology Society, 2008. EMBS 2008. 30th Annual International Conference of the IEEE*, pages 3241–3244. IEEE, 2008.

[35] A. Talasaz, RV Patel, and MD Naish. Haptics-enabled teleoperation for robot-assisted tumor localization. In *Robotics and Automation (ICRA), 2010 IEEE International Conference on*, pages 5340–5345. IEEE, 2010.

[36] Y. Kasahara, K. Kitamura, K. Ohnishi, Y. Morikawa, and N. Shimojima. Rupture detection for exenteration of tissues using two-dof haptic surgical forceps robot. In *Advanced Motion Control, 2010 11th IEEE International Workshop on*, pages 284–289. IEEE, 2010.

[37] J. Zhu, X. He, and W. Gueaieb. Trends in the control schemes for bilateral teleoperation with time delay. *Autonomous and Intelligent Systems*, pages 146–155, 2011.

[38] A. Gasparetto, R. Vidoni, and V. Zanotto. Dforce: Delayed force reference control for master-slave robotic systems. *Mechatronics*, 19(5):639–646, 2009.

[39] U. Hagn, M. Nickl, S. Jorg, G. Passig, T. Bahls, A. Nothhelfer, F. Hacker, L. Le-Tien, A. Albu-Schaffer, R. Konietschke, et al. The dlr miro: a versatile lightweight robot for surgical applications. *Industrial Robot*, 35(4):324–336, 2008.

[40] R. Bischoff, J. Kurth, G. Schreiber, R. Koeppe, A. Albu-Schäffer, A. Beyer, O. Eiberger, S. Haddadin, A. Stemmer, G. Grunwald, et al. The kuka-dlr lightweight robot arm-a new reference platform for robotics research and manufacturing. In *Robotics (ISR), 2010 41st International Symposium on and 2010 6th German Conference on Robotics (ROBOTIK)*, pages 1–8. VDE, 2010.

[41] H. Mönnich, D. Stein, J. Raczkowsky, and H. Wörn. A hand guided robotic planning system for laser osteotomy in surgery. In *World Congress on Medical Physics and Biomedical Engineering, September 7-12, 2009, Munich, Germany*, pages 59–62. Springer, 2009.

[42] M. Rajh, S. Glodez, J. Flasker, K. Gotlih, and T. Kostanjevec. Design and analysis of an fmri compatible haptic robot. *Robotics and Computer-Integrated Manufacturing*, 27(2):267–275, 2011.

[43] U. Hagn, T. Ortmaier, R. Konietschke, B. Kubler, U. Seibold, A. Tobergte, M. Nickl, S. Jorg, and G. Hirzinger. Telemanipulator for remote minimally invasive surgery. *Robotics & Automation Magazine, IEEE*, 15(4):28–38, 2008.

[44] S.L. Lee, M. Lerotic, V. Vitiello, S. Giannarou, K.W. Kwok, M. Visentini-Scarzanella, and G.Z. Yang. From medical images to minimally invasive intervention: Computer assistance for robotic surgery. *Computerized Medical Imaging and Graphics*, 34(1):33–45, 2010.

[45] P. Gomes. Surgical robotics: Reviewing the past, analysing the present, imagining the future. *Robotics and Computer-Integrated Manufacturing*, 27(2):261–266, 2011.

[46] H. Tanaka, K. Ohnishi, H. Nishi, T. Kawai, Y. Morikawa, M. Kitajima, S. Ozawa, and T. Furukawa. Bilateral control in multi dof haptic surgical robotic system utilizing fpga. In *Industrial Electronics, 2007. ISIE 2007. IEEE International Symposium on*, pages 3084–3089. IEEE, 2007.

[47] T. Beyl, P. Nicolai, H. Mönnich, J. Raczkowksy, and H. Wörn. Haptic feedback in op: Sense-augmented reality in telemanipulated robotic surgery. *Studies in health technology and informatics*, 173:58, 2012.

[48] A. Tobergte, R. Konietschke, and G. Hirzinger. Planning and control of a teleoperation system for research in minimally invasive robotic surgery. In *Robotics and Automation, 2009. ICRA'09. IEEE International Conference on*, pages 4225–4232. IEEE, 2009.

[49] B. Bäuml and G. Hirzinger. When hard realtime matters: Software for complex mechatronic systems. *Robotics and Autonomous Systems*, 56(1):5–13, 2008.

[50] G.Y. Tan, R.K. Goel, J.H. Kaouk, and A.K. Tewari. Technological advances in robotic-assisted laparoscopic surgery. *Urologic Clinics of North America*, 36(2):237–249, 2009.

[51] S.J. Phee, S.C. Low, VA Huynh, A.P. Kencana, ZL Sun, and K. Yang. Master and slave transluminal endoscopic robot (master) for natural orifice transluminal endoscopic surgery (notes). In *Engineering in Medicine and Biology Society, 2009. EMBC 2009. Annual International Conference of the IEEE*, pages 1192–1195. IEEE, 2009.

[52] K. Yang, ZL Sun, AP Kencana, VA Huynh, M. Rasouli, SJ Phee, D. Lomanto, and KY Ho. Enhancement of spatial orientation and haptic perception for master-slave robotic natural orifice transluminal endoscopic surgery (notes). In *Robotics Automation and Mechatronics (RAM), 2010 IEEE Conference on*, pages 15–18. IEEE, 2010.

[53] A.L. Trejos, J. Jayender, MT Perri, MD Naish, RV Patel, and RA Malthaner. Robot-assisted tactile sensing for minimally invasive tumor localization. *The International Journal of Robotics Research*, 28(9):1118–1133, 2009.

[54] J.W. Park, J. Choi, H.N. Pak, S.J. Song, J.C. Lee, Y. Park, S.M. Shin, and K. Sun. Development of a force-reflecting robotic platform for cardiac catheter navigation. *Artificial Organs*, 34(11):1034–1039, 2010.

[55] L. Cercenelli, E. Marcelli, and G. Plicchi. Initial experience with a telerobotic system to remotely navigate and automatically reposition standard steerable ep catheters. *ASAIO Journal*, 53(5):523, 2007.

[56] Stephanie Dionne Sherk. Microsurgery. `http://www.surgeryencyclopedia.com/La-Pa/Microsurgery.html`. Accessed May 19, 2012.

[57] R. Taylor, P. Jensen, L. Whitcomb, A. Barnes, R. Kumar, D. Stoianovici, P. Gupta, Z.X. Wang, E. Dejuan, and L. Kavoussi. A steady-hand robotic system for microsurgical augmentation. *The International Journal of Robotics Research*, 18(12):1201–1210, 1999.

[58] M.J. Lang, A.D. Greer, and G.R. Sutherland. Intra-operative robotics: Neuroarm. *Intraoperative Imaging*, pages 231–236, 2011.

[59] T. Tuytelaars and K. Mikolajczyk. Local invariant feature detectors: a survey. *Foundations and Trends in Computer Graphics and Vision*, 3(3):177–280, 2008.

[60] K. Mikolajczyk and C. Schmid. A performance evaluation of local descriptors. *Pattern Analysis and Machine Intelligence, IEEE Transactions on*, 27(10):1615–1630, 2005.

[61] K. Mikolajczyk, T. Tuytelaars, C. Schmid, et al. Affine covariant features. *Collaborative work between: the Visual Geometry Group, Katholieke Universiteit Leuven, Inria Rhone-Alpes and the Center for Machine Perception*, 2007.

[62] H. Bay, T. Tuytelaars, and L. Van Gool. Surf: Speeded up robust features. *Computer Vision–ECCV 2006*, pages 404–417, 2006.

[63] M. Heikkilä, M. Pietikäinen, and C. Schmid. Description of interest regions with local binary patterns. *Pattern recognition*, 42(3):425–436, 2009.

[64] F. Bellavia, D. Tegolo, and E. Trucco. Improving sift-based descriptors stability to rotations. In *Proceedings of the 2010 20th International Conference on Pattern Recognition*, pages 3460–3463. IEEE Computer Society, 2010.

[65] S. Leutenegger, M. Chli, and R.Y. Siegwart. Brisk: Binary robust invariant scalable keypoints. In *Computer Vision (ICCV), 2011 IEEE International Conference on*, pages 2548–2555. IEEE, 2011.

[66] F. Fraundorfer and H. Bischof. A novel performance evaluation method of local detectors on non-planar scenes. In *Computer Vision and Pattern Recognition-Workshops, 2005. CVPR Workshops. IEEE Computer Society Conference on*, pages 33–33. IEEE, 2005.

[67] S. Gauglitz, T. Höllerer, and M. Turk. Evaluation of interest point detectors and feature descriptors for visual tracking. *International journal of computer vision*, pages 1–26, 2011.

[68] A. Alahi, L. Bagnato, D. Matti, and P. Vandergheynst. Foreground silhouettes extraction robust to sudden changes of background appearance. In *IEEE International conference on Image Processing*, 2012.

[69] K. Mikolajczyk and C. Schmid. An affine invariant interest point detector. *Computer Vision,ECCV 2002*, pages 128–142, 2002.

[70] G. Bradski. The opencv library. *Dr. Dobb's Journal of Software Tools*, 2000.

[71] R. Hartley and A. Zisserman. *Multiple View Geometry in Computer Vision*. Cambridge University Press, second edition, 2004.

[72] G.B. Hughes and M. Chraibi. Calculating ellipse overlap areas. `http://works.bepress.com/gbhughes/17/`, 2011.

[73] L.A. Piegl and W. Tiller. *The NURBS book*. Springer Verlag, 1997.

[74] O. Ruiz, C. Vanegas, and C. Cadavid. Ellipse-based principal component analysis for self-intersecting curve reconstruction from noisy point sets. *The visual computer*, pages 1–16, 2011.

[75] W.D. Ueng, J.Y. Lai, and Y.C. Tsai. Unconstrained and constrained curve fitting for reverse engineering. *The International Journal of Advanced Manufacturing Technology*, 33(11):1189–1203, 2007.

[76] T.F. Edgar, D.M. Himmelblau, and L.S. Lasdon. *Optimization of chemical processes*. McGraw-Hill, 2001.

[77] J. Nocedal and S. Wright. Numerical optimization, series in operations research and financial engineering, 2006.

[78] A.V. Fiacco. *Introduction to sensitivity and stability analysis in nonlinear programming*. Academic Press, 1983.

[79] C.H. Papadimitriou and K. Steiglitz. *Combinatorial optimization: algorithms and complexity*. Dover Publications, 1998.

[80] S. Flöry and M. Hofer. Surface fitting and registration of point clouds using approximations of the unsigned distance function. *Computer Aided Geometric Design*, 27(1):60–77, 2010.

[81] W. Wang, H. Pottmann, and Y. Liu. Fitting b-spline curves to point clouds by curvature-based squared distance minimization. *ACM Transactions on Graphics (TOG)*, 25(2):214–238, 2006.

[82] Y. Liu, H. Yang, and W. Wang. Reconstructing b-spline curves from point clouds–a tangential flow approach using least squares minimization. In *Shape Modeling and Applications, 2005 International Conference*, pages 4–12. IEEE, 2005.

[83] A. Gálvez, A. Iglesias, A. Cobo, J. Puig-Pey, and J. Espinola. Bézier curve and surface fitting of 3d point clouds through genetic algorithms, functional networks and least-squares approximation. *Computational Science and Its Applications–ICCSA 2007*, pages 680–693, 2007.

[84] Y. Liu and W. Wang. A revisit to least squares orthogonal distance fitting of parametric curves and surfaces. *Advances in Geometric Modeling and Processing*, pages 384–397, 2008.

[85] S. Flöry and M. Hofer. Constrained curve fitting on manifolds. *Computer-Aided Design*, 40(1):25–34, 2008.

[86] S. Flöry. Fitting curves and surfaces to point clouds in the presence of obstacles. *Computer Aided Geometric Design*, 26(2):192–202, 2009.

[87] E. Saux and M. Daniel. An improved hoschek intrinsic parametrization. *Computer Aided Geometric Design*, 20(8-9):513–521, 2003.

[88] A. Blake and M. Isard. *Active contours: the application of techniques from graphics, vision, control theory and statistics to visual tracking of shapes in motion*. Springer, 1998.

[89] H. Yang, W. Wang, and J. Sun. Control point adjustment for b-spline curve approximation. *Computer-Aided Design*, 36(7):639–652, 2004.

[90] W. Heidrich, R. Bartels, and G. Labahn. Fitting uncertain data with nurbs. In *Proceedings of* 3^{rd} *Int. Conf. on Curves and Surfaces in Geometric Design*, pages 1–8. Vanderbilt University Pres, 1996.

[91] D. Pekerman, G. Elber, and M.S. Kim. Self-intersection detection and elimination in freeform curves and surfaces. *Computer-Aided Design*, 40(2):150–159, 2008.

[92] O. Ruiz and P. Ferreira. Algebraic Geometry and Group Theory in Geometric Constraint Satisfaction for Computer Aided Design and Assembly Planning. *IIE Transactions. Focussed Issue on Design and Manufacturing*, 28(4):281–204, 1996.

[93] D. Kapur and Y. Lakshman. *Elimination Methods: An Introduction*, pages 45–88. Academic Press, 1992.